Yang *et al. Energy Mater* 2023;3:300042
DOI: 10.20517/energymater.2023.29

Energy Materials

Review

Open Access

Check for updates

Recent progress on metal-organic framework derived carbon and their composites as anode materials for potassium-ion batteries

Lei Yang[1], Jingwei Chen[1,*], Sangbaek Park[2], Huanlei Wang[1,*]

[1]School of Materials Science and Engineering, Ocean University of China, Qingdao 266100, Shandong, China.
[2]Department of Materials Science and Engineering, Chungnam National University, Yuseong-gu, Daejeon 34134, Republic of Korea.

***Correspondence to:** Prof./Dr. Jingwei Chen, School of Materials Science and Engineering, Ocean University of China, No. 1299, Sansha Road, West Coast New District, Qingdao 266100, Shandong, China. E-mail: chenjingwei@ouc.edu.cn; Prof./Dr. Huanlei Wang, School of Materials Science and Engineering, Ocean University of China, No. 1299, Sansha Road, West Coast New District, Qingdao 266100, Shandong, China. E-mail: huanleiwang@ouc.edu.cn

How to cite this article: Yang L, Chen J, Park S, Wang H. Recent progress on metal-organic framework derived carbon and their composites as anode materials for potassium-ion batteries. *Energy Mater* 2023;3:300042. https://dx.doi.org/10.20517/energymater.2023.29

Received: 24 Apr 2023 **First Decision:** 8 Jun 2023 **Revised:** 22 Jun 2023 **Accepted:** 6 Jul 2023 **Published:** 8 Oct 2023

Academic Editors: Yuping Wu, Federico Bella **Copy Editor:** Fangling Lan **Production Editor:** Fangling Lan

Abstract

Potassium-ion batteries (PIBs) are considered as promising alternatives to lithium-ion batteries (LIBs) due to their abundant potassium resources, cost-effectiveness, and comparable electrochemical performance to LIBs. However, the practical application of PIBs is hindered by the slow dynamics and large volume expansion of anode materials. Owing to their unique morphology, rich pores, abundant active sites, and tunable composition, metal-organic framework (MOF)-derived carbon and its composites have been widely studied and developed as PIB anodes. In this review, the basic configuration, performance evaluation indicators, and energy storage mechanisms of PIBs were first introduced, followed by a comprehensive summary of the research progress in MOF-derived carbon and its composites, especially the design strategies and different types of composites. Moreover, the advances of *in situ* characterization techniques to understand the electrochemical mechanism during potassiation/depotassiation were also highlighted, which is crucial for the directional optimization of the electrochemical performance of PIBs. Finally, the challenges and development prospects of MOF-derived carbon and its composites for PIBs are prospected. It is envisioned that this review will guide and inspire more research efforts toward advanced MOF-derived PIB anode materials in the future.

Keywords: Metal-organic framework-derived carbon, carbon composites, *in situ* characterization, potassium-ion batteries

INTRODUCTION

The massive consumption of limited fossil fuels over the past decades, accompanied by excessive carbon emissions, has led to environmental pollution and a potential energy crisis, endangering the sustainable development and survival of mankind[1-3]. The international focus on reducing carbon emissions to achieve carbon neutrality has prompted researchers to harvest clean and renewable energies in nature, such as wind, solar, and tidal energy[4-7]. However, wide utilization of these intermittent energies is restricted due to their dependence on climate and region. Therefore, it is extremely urgent to develop efficient and economical energy conversion and storage devices. Lithium-ion batteries (LIBs) have been successfully commercialized in portable charging devices and electric vehicles due to their high energy density, fast charging/discharging, and long cycle life[8-12]. Unfortunately, the deficiency and uneven geographical distribution of lithium (Li) resources have caused the rising cost of LIBs, which compromised their competitiveness in the large-scale economic energy storage market[13-15]. Sodium (Na), a neighboring element of Li, has received plentiful attention because the content of Na (2.3%) is much higher than that of Li (0.0017%) in the earth's crust[16,17]. In addition, the similar physicochemical properties of Na with Li drive the research of sodium-ion batteries (SIBs)[18,19]. Regrettably, the energy density of SIBs is relatively lower than that of LIBs due to the higher standard reduction potential of Na compared to Li[20]. Potassium-ion batteries (PIBs) are considered as another alternative to LIBs due to their abundant potassium (K) resources (1.5%) and lower costs[21-23]. Figure 1A shows the physicochemical parameters of Li, Na, and K. Compared to SIBs, PIBs possess the following merits: (i) The standard reduction potential of K (-2.93 V *vs.* standard hydrogen electrodes (SHE)) is lower than Na (-2.71 V *vs.* SHE) and closer to Li (-3.04 V *vs.* SHE), endowing PIBs with relatively wide operating voltage and high energy density[24]; (ii) The Stokes radius of K ions (3.6 Å) in propylene carbonate (PC) is smaller than that of Na and Li ions (4.6 Å and 4.8 Å), ensuring their good ionic conductivity and fast kinetics[20]; and (iii) Aluminum (Al) foil can be employed as the current collector of PIBs because K will not react with Al, and the cost of PIB electrolyte salts is lower than that of SIBs, thus greatly reducing the cost of PIBs[25]. Based on the above advantages, PIBs have been considered as the most competitive candidates for next-generation large-scale energy storage devices.

Similar to LIBs, PIBs are typical rocking chair batteries and are mainly constituted of cathodes, electrolytes, and anodes. Owing to the large K ion radius, advanced anode materials play a key role in improving the electrochemical performance of PIBs. Since it was verified that the K ion can be inserted into and extracted from the graphitic layer ($KC_{36} \leftrightarrow KC_{24} \leftrightarrow KC_8$), and commercial graphite anodes can achieve a capacity of 273 mAh g^{-1}[26], the number of publications involving anode materials and PIBs has rapidly increased in recent years [Figure 1B]. At present, various anode materials, such as carbon, metal compounds, alloying materials, and their composites, have been synthesized and applied to improve the electrochemical performance of PIBs[27-29]. Generally, carbon materials are ideal anode materials for PIBs owing to their low cost and excellent physicochemical properties. Rational structure design and doping engineering can effectively enhance their potassium storage performance[30-32]. In addition, conversion-type materials (such as metal compounds) and alloying-type materials (such as Bi and P) have been investigated as anodes for PIBs due to their high theoretical capacity. Unfortunately, these materials have inferior cyclic performance due to tremendous volume expansion during potassiation. Therefore, composite materials combining carbon materials and conversion/alloying-type materials have been investigated[33-35]. Although progress has been achieved, it is still an enormous challenge to synchronously harvest the merits of both carbon and conversion/alloying-type materials through structural design, doping engineering, and the formation of composites.

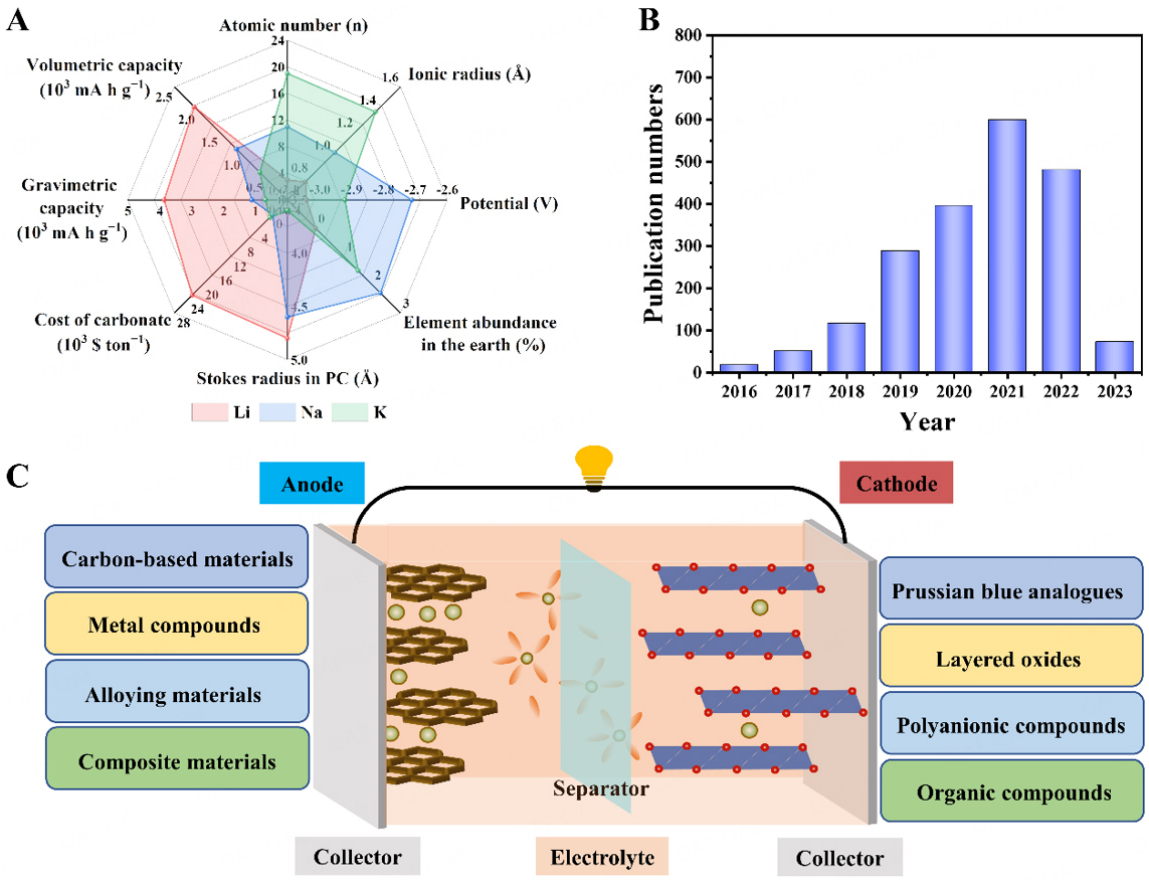

Figure 1. (A) Comparison of physicochemical parameters of Li, Na, and K. (B) Publication numbers related to anode materials of PIBs. The data come from the Web of Science with the keywords including "anode materials" and "potassium-ion batteries" (accessed on 1 March 2023). (C) Illustration of the configuration of PIBs.

Metal-organic frameworks (MOFs), composed of metal ions and organic ligands through covalent coordination, have harvested extensive attention as a new kind of porous material due to their different morphologies, adjustable pore structures, and abundant active sites[36-40]. Owing to their controllable structure and tunable composition, MOFs have been employed to derive carbon materials with large specific surface area, well-developed pores, and high levels of heteroatom doping by carbonization and acid etching[41,42]. Moreover, MOF-derived carbon composites can be obtained through facile synthesis strategies. Recently, Cao *et al.* reported a novel space-confined method that successfully confined different metal ions (Mg^{2+}, Al^{3+}, Ca^{2+}, Ti^{4+}, Mn^{2+}, Fe^{3+}, Ni^{2+}, Zn^{2+}, Pb^{2+}, Ba^{2+}, and Ce^{4+}) in quasi-microcube shaped cobalt (Co) benzimidazole frameworks (CoZIF9)[43]. The original framework of CoZIF9 will not be destroyed by metal ion addition when the ratio of Co to metal ions is optimized to 10/1. Excitingly, a series of MOF-derived carbon prepared through high-temperature carbonization exhibited excellent electrochemical performance. Based on the above advantages, MOF-derived carbon and its composites have been comprehensively applied in LIBs and SIBs and are gradually adopted in PIBs in recent years[44-46]. For example, Jiang *et al.* confined $Sn_3(PO_4)_2$ nanocrystals in an interconnected carbon framework through a controllable particle attachment crystallization growing process of Sn-based phosphate MOFs and high-temperature calcination strategies[47]. The as-fabricated composite exhibited appreciable electrochemical performance as both SIB and PIB anodes. Therefore, it is necessary to summarize the recent progress of MOF-derived carbon and its composites in PIBs. To our knowledge, most of the previous reviews on PIB anodes focused on the classification and optimization of carbon materials[21,22,48] or the type and regulation of metal compounds[5,28],

but few reviews on MOF-derived carbon and its composites[37,49]. In this review, we first briefly introduce the configuration, performance evaluation indicators, and energy storage mechanisms of PIBs. Then, we comprehensively summarize the research progress of MOF-derived carbon and its composites as PIB anodes, especially the design strategies and composite types. Furthermore, the importance and necessity of advanced characterization techniques are highlighted for understanding potassium storage mechanisms. Finally, we put forward the challenges and development prospects of MOF-derived carbon and its composites for PIBs. We aspire that this review will guide and inspire more research efforts toward advanced MOF-derived PIB anode materials in the future.

A BRIEF INTRODUCTION OF PIBS

Basic configuration

As shown in Figure 1C, PIBs are mainly composed of cathodes, anodes, electrolytes, and separators. Generally, the cathode determines the maximum operating voltage of PIBs, but it provides a lower capacity than the anode. Considering the intercalation-dominated reaction of large radius K ion, cathode materials with rigid structures and large channels are favorable for reversible K ion intercalation/deintercalation. At present, PIB cathodes mainly include Prussian blue analogs, layered oxides, polyanionic compounds, and organic compounds[50,51]. As the counterpart of a cathode, an anode is another important component of PIBs. Due to the low standard reduction potential and high theoretical capacity, potassium metal is the ultimate anode for PIBs. Notwithstanding, the practical application of potassium metal is difficult, as its high reactivity with electrolytes and water will cause poor cycle efficiency and serious safety hazards. Therefore, other advanced anode materials, including carbon-based materials, metal compounds, alloying materials, and their composites, are to be developed[52,53]. Electrolytes also play a crucial role in PIBs because the utilization of inappropriate electrolytes will not only deteriorate the performance of PIBs but also may promote the dendrite growth and formation of uneven solid electrolyte interface (SEI) layers, causing safety problems. Generally, an excellent electrolyte should have wide working potential window, high ionic conductivity, and so on. To date, commonly used PIB electrolytes are organic electrolytes composed of ethylene carbonate (EC), diethyl carbonate (DEC), dimethyl carbonate (DMC), ethyl methyl carbonate (EMC), ethylene glycol dimethyl ether (DME) or diethylene glycol dimethyl ether (DEGDME) solvents, and potassium hexafluorophosphate (KPF_6) or potassium bis(fluorosulfonyl)imide (KFSI) salts[54-58]. Finally, the separator should ensure the free shuttle of electrolyte ions between cathodes and anodes and prevent the battery short circuit caused by the growing potassium dendrites penetrating the separator. A thick Whatman glass fiber filter is usually applied as the PIB separator[59,60].

Performance evaluation indicators

The electrochemical performance of energy storage devices should be comprehensively evaluated before commercialization. Generally, PIBs can be evaluated by specific capacity, working voltage, rate capability, energy density, power density, cycle stability, and Coulombic efficiency (CE), *etc*.[22,48] Among them, the specific capacity is the most intuitive indicator to reflect the potassium storage capability of electrodes, which also determines the energy density of PIBs. Working voltage is another decisive factor affecting the energy density of PIBs, which can be enhanced through electrolyte optimization. Therefore, to achieve PIBs with high energy density, high-potential cathodes with high capacity are to be coupled with low-potential anodes. Power density determines the speed at which PIBs store/release energy, which is related to rate capability. Considering the fast kinetics of a capacitive process, rational design of anode materials with higher contributions of capacitive behavior is an effective strategy to improve rate capability and power density[61]. In addition, cycle stability is another key indicator determining the commercialization process of PIBs, which is mainly related to the structural stability of electrodes and electrolytes and the electrode-electrolyte interface. CE refers to the ratio of released to stored potassium ions, which is calculated from the ratio of charge to discharge capacity in the same cycle[62,63]. When CE is less than 100%, it means that the

anode is constantly trapping limited K ions, which is not conducive to the commercial application of PIBs. The first discharge will form a stable SEI and lead to poor initial CE (ICE), which is also an important indicator for evaluating PIBs.

Energy storage mechanisms

Similar to LIBs and SIBs, PIBs are also typical rocking chair batteries[64,65]. Generally, the main K ion storage mechanism in the cathode is intercalation. On the contrary, the storage mechanisms of K ion at the anode mainly include intercalation, adsorption, conversion, and alloying reactions[22]. The intercalation reaction is often observed in layered materials (such as graphite), which usually deliver a capacity of less than 300 mAh g^{-1}[26,66]. The capacity of carbon nanomaterials with high specific surface area and rich active sites can be improved by enhanced adsorption reaction[67-69]. The conversion reaction usually occurs in metal compounds[70,71]. Compared with intercalation reaction and adsorption reaction, conversion reaction-based anodes usually have higher K ion storage capacity but are often accompanied by large volume change, leading to poor cycle performance. Additionally, Some Bi-, Sn-, and P-based materials that can form alloys upon potassiation often exhibit superior K ion storage capacity through alloying reaction[72-74]. Generally, composites with mixed K ion storage mechanisms have been designed and synthesized to improve the overall performance of PIBs. In addition to the above reaction mechanisms, there are two K ion storage behaviors in anodes: surface-induced capacitive behavior (SCB) and diffusion-controlled intercalation behavior (DIB)[75,76]. The SCB refers to reversible physical/chemical adsorption of K ion in nanopores, defects, and functional groups, while the DIB is related to a Faradaic reaction of potassiation. The SCB and DIB can be qualitatively analyzed by the formula $i = av^b$, in which i and v represent peak current and scanning rate, respectively, and the b-value determines the storage behavior of K ion. The b-value close to 1 (SCB-dominated K ion storage) rather than 0.5 (DIB-dominated K ion storage) indicates fast kinetics and higher SCB contributions to K ion storage capacity. Besides, the SCB contribution can be further quantified by the formula $i = k_1v + k_2v^{1/2}$, in which k_1v and $k_2v^{1/2}$ represent the SCB and DIB contribution, respectively.

MOF-DERIVED CARBON AND ITS COMPOSITES FOR PIB ANODES

Based on the above discussion, PIBs are expected to implement LIBs due to the abundant and evenly distributed potassium resources and low prices of potassium carbonate and aluminum current collectors. In order to overcome the rapid electrochemical performance degradation of PIBs caused by large K ions during cycling, a series of anode materials have been designed and synthesized. It has been proved that rational design of carbon materials can observably improve the potassium storage performance. By intelligently adjusting the pore structure of carbon materials, ions/electrons transmission can be promoted, and volume change can be mitigated, thus improving potassium storage performance. Heteroatom doping is another method to significantly improve potassium storage performance via adjusting the electronic structure to increase the conductivity and wettability and expand the layer spacing. In addition, the construction of carbon-based composite materials with conversion/alloy-based materials is also a significant strategy through synergistic effects. Thanks to the diversified selection of metal sources (such as Zn and Co), organic ligands (such as 2-methylimidazole and terephthalic acid), and solvents (such as deionized water and methanol), the prepared MOF-derived carbon possesses the advantages of controlled structure and abundant heteroatoms[77,78]. Furthermore, the composite materials can be facilely prepared from pristine MOFs with abundant carbon/heteroatom/metal ions. Therefore, MOF-derived carbon and its composites have received increasing attention as PIB anodes. In this section, we summarize the rational design strategies of MOF-derived carbon and the progress in different types of MOF-derived carbon composites [Figure 2].

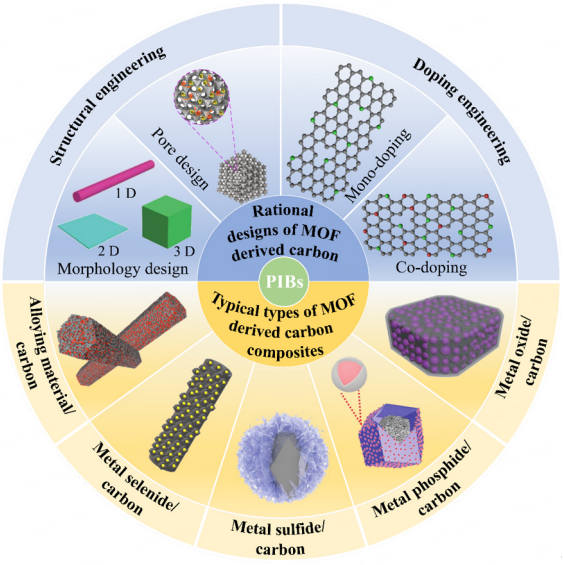

Figure 2. Schematic of the rational design strategies of MOF-derived carbon and typical types of MOF-derived carbon composites.

Rational design of MOF-derived carbon

The structure of MOF-derived carbon is a key factor affecting the potassium storage performance. The structural characteristics, such as morphology, pore size/volume, interlayer spacing, and specific surface area, greatly affect electron transmission, ion diffusion, volume expansion, and effective contact area with electrolyte, which further determines the capacity, CE, rate capability, and cycle ability of PIBs. In addition, the introduction of heteroatoms can adjust the electronic structure, number of defects, layer spacing, and wettability of MOF-derived carbon anodes so as to achieve good potassium storage performance. Herein, we mainly discuss the influence of structural engineering (morphology/pore design) and doping engineering (mono-/co-doping) of MOF-derived carbon anodes.

Structural engineering (morphology design)

The morphology of MOF-derived carbon can generally be divided into one-, two- and three-dimensional (1, 2, and 3D) nanostructures. 1D nanostructures refer to structures, such as nanofibers, nanowires, nanotubes, and nanorods, which can rapidly transfer electrons. A zeolitic imidazolate framework (ZIF), as a typical MOF, has been used to synthesize carbon with unique structures. For example, Xiong *et al.* prepared 1D N-doped carbon nanotubes (NCNTs) with an average outer diameter of approximately 20 nm through simple and high-yield high-temperature calcination of ZIF-67, which delivered a high capacity of 300.7 mAh g^{-1} as PIB anodes[79]. 2D nanostructures have directional layered carbon sheets, which not only ensure the full contact between electrolyte/electrode but also effectively mitigate the volume change during potassiation. Li *et al.* prepared 2D amorphous carbon/graphitic carbon nanoplates from Zn-MOF@Co-MOF[80]. In addition, other 2D MOF-derived carbon materials, including carbon-onion-constructed nanosheets[81], Mn-MOF-derived carbon microsheets[82], and 2D Cu-MOF-derived carbon sheets[83], have been prepared and deliver excellent potassium storage properties.

Apart from 1D and 2D nanostructures, MOF-derived carbon with 3D networks usually shows increased layer spacing for K ion storage and interconnected highways for electron conduction, thus improving the rate performance. Zhang *et al.* synthesized ZIF-67-derived 3D graphitic carbon networks, exhibiting excellent potassium storage properties with good rate capability and long cycle life[84]. Li *et al.* synthesized S-doped ZIF-67-derived carbon microboxes with an expanded interlayer distance, which is conducive to K

ion insertion/extraction[85]. Thus, the as-prepared carbon anode delivered good cycle life. In addition, MOF-derived carbon with core-shell nanostructures has been widely studied due to its unique merits[86]. For PIBs, core-shell nanostructures can not only increase more active sites but also speed up reaction kinetics. Yu *et al.* successfully synthesized ten different Ni/Co-MOF@ZIF core-shell materials by helical chains and 2,5-dihydroxybenzenedicarboxylate (DHBDC), including 3D nanoparticles, 2D nanosheets, and 1D nanowires, as shown in transmission electron microscope (TEM) images [Figure 3A][87]. After high-temperature carbonization and etching, the prepared carbon materials retained the core-shell structure of the pristine MOFs, as displayed in scanning electron microscopy (SEM) images [Figure 3B]. Electrochemical tests had verified the improved potassium storage performance of all core-shell MOF-derived carbon than that of single MOF-derived carbon.

Structural engineering (pore design)

MOF-derived carbon often contains abundant nanopores, either open or closed. Open pores can increase the specific surface area, while closed pores can provide active sites. According to the pore size (d), the pores in carbon materials can be divided into macropores (d > 50 nm), mesopores (2 nm < d < 50 nm), and micropores (d < 2 nm)[22,48]. Macropores can be used as buffer reservoirs for electrolytes, mesopores can be used as diffusion channels for electrolyte ions, and micropores can be used for capacitive storage of K ions. Therefore, rational pore structure design of MOF-derived carbon is important to improve its potassium storage performance.

Thanks to the unique porous properties of MOFs, MOF-derived carbon also has rich pore structures. For instance, Liang *et al.* synthesized 3D Al-MOF with a nanorod-assembly structure by precisely adjusting the nucleation and growth process of MOFs [Figure 3C][88]. The N-doped carbon nanorod-assembled superstructures (NCS) obtained after pyrolysis and etching possessed rich micropores, with micropore area of up to 915.1 $m^2 g^{-1}$, which is 63% of the total surface area. Compared with the potassiation of a graphite anode, abundant micropores in NCS can capture a large number of K ions at a voltage above 0.4 V [Figure 3D]. As a result, the NCS anode displayed a high capacity [Figure 3E]. However, excess micropores will prolong the time for electrolyte infiltration, thus forming a thicker SEI layer, resulting in active K ions loss. Thus, the properly controlled formation of micropores can increase the CE of PIBs. Yuan *et al.* successfully prepared superstructure carbon materials (SCNSs) through pyrolysis of mixed ZIF-8 and polyvinylpyrrolidone (PVP)[89]. Due to the preferential decomposition of external PVP, the as-prepared SCNSs presented a mesopores-dominated pore structure, which greatly shortened the ion diffusion distance and inhibited the loss of active K ions. Accordingly, the SCNS anode achieved an outstanding rate capacity and cycling life.

In addition to single dominant pores, carbon anodes with hierarchical pore structures of macropore, mesopore, and micropore often show excellent potassium storage performance. Zhou *et al.* synthesized interconnected N-doped hierarchical porous carbon (N-HPC) by carbonizing the well-designed ZIF-8[90]. The interconnected structure and hierarchical pores promoted the transfer of electrons and ions, respectively. Thus, the N-HPC anode delivered an excellent reversible capacity and superior rate performance. Ruan *et al.* constructed N-doped microporous carbon polyhedrons (NMCP), which were further wrapped by reduced graphene oxide (NMCP@rGO)[91]. Figure 3F illustrated that the NMCP@rGO possessed 3D NMCP with rich micropores as the interior carbon and 2D rGO with mesopores and macropores as the outer carbon. Therefore, the NMCP@rGO exhibited a multi-dimensional double carbon structure with hierarchical pores [Figure 3G], which delivered excellent potassium storage performance.

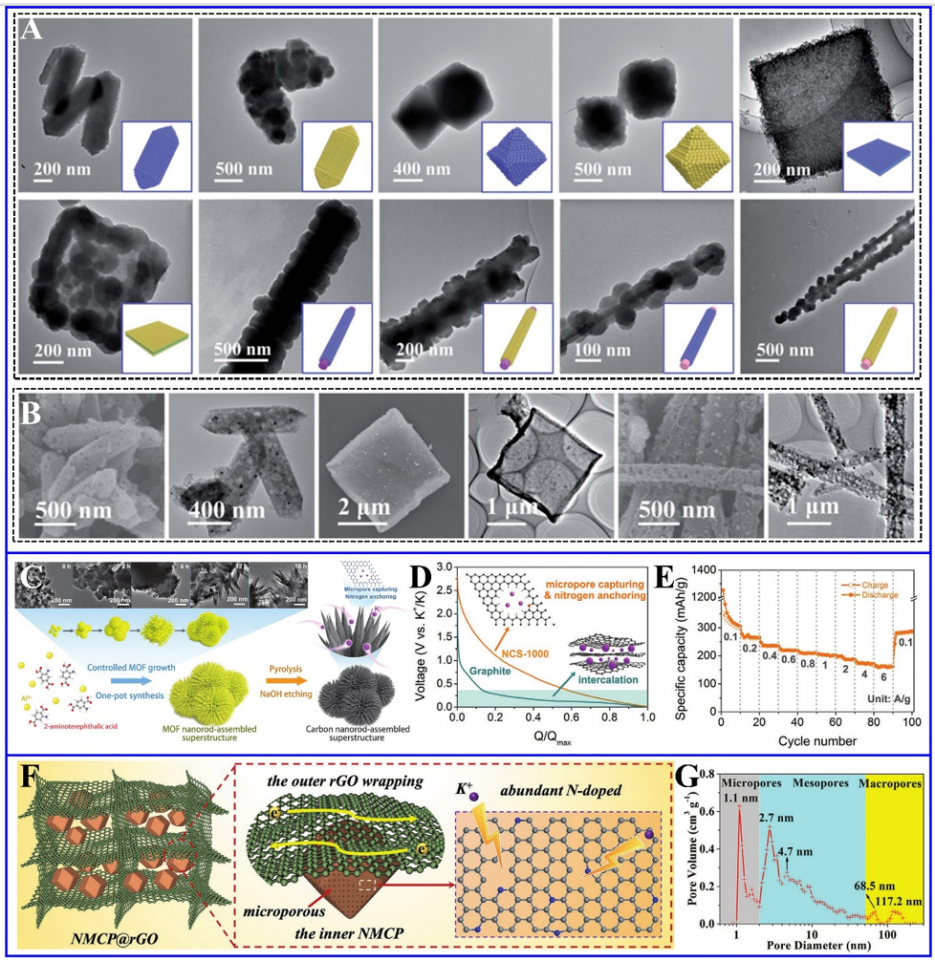

Figure 3. (A) TEM images of core-shell MOF hybrids with various morphologies and (B) SEM images of carbon derived from them. This figure is quoted with permission from Yu *et al.*[87]. (C) Schematic of the synthesis process, (D) discharge curve, and (E) rate performance of NCS. This figure is quoted with permission from Liang *et al.*[88]. (F) Structure schematic and (G) pore size distribution of NMCP@rGO. This figure is quoted with permission from Ruan *et al.*[91].

Doping engineering (mono-doping)

N is one of the most commonly used doping elements to enhance potassium storage performance in carbon materials. Generally, N species are divided into pyridine N (N-6), pyrrolic N (N-5), and quaternary N (N-Q)[92]. N-6 and N-5 can function as electrochemical sites to enhance the SCB of K ions, which is conducive to capacity improvement. N-Q bonds with three sp^2 carbon atoms, which is beneficial for improving conductivity[93]. Encouragingly, 2-methylimidazole of ZIF-67 and ZIF-8 contain abundant and various N chemical bonds, which can be decomposed under different calcination temperatures and *in situ* produce different N species. Therefore, ZIF-67 and ZIF-8 are often used to prepare N-doped MOF-derived carbon. Li *et al.* prepared N-doped porous carbon (NPC) with controllable N-6 content by optimizing the carbonization temperature [Figure 4A][94]. The as-prepared NPC retained the polyhedron morphology of the precursor with abundant pores. When the calcination temperature was 600 °C, the as-prepared NPC-600 had the highest level of N-6 among all samples [Figure 4B]. MET-6, a MOF composed of Zn^{2+} and N-rich 1H-1,2,3-triazole ligands (60 wt.% N), was used as C and N precursors to synthesize the NPC framework with the N level of up to 13.57%[95]. The as-prepared sample achieved an excellent potassium storage performance. Moreover, the density functional theory (DFT) was used to further understand the advantages of N doping in enhancing the potassium storage properties. The K ion adsorption energies of

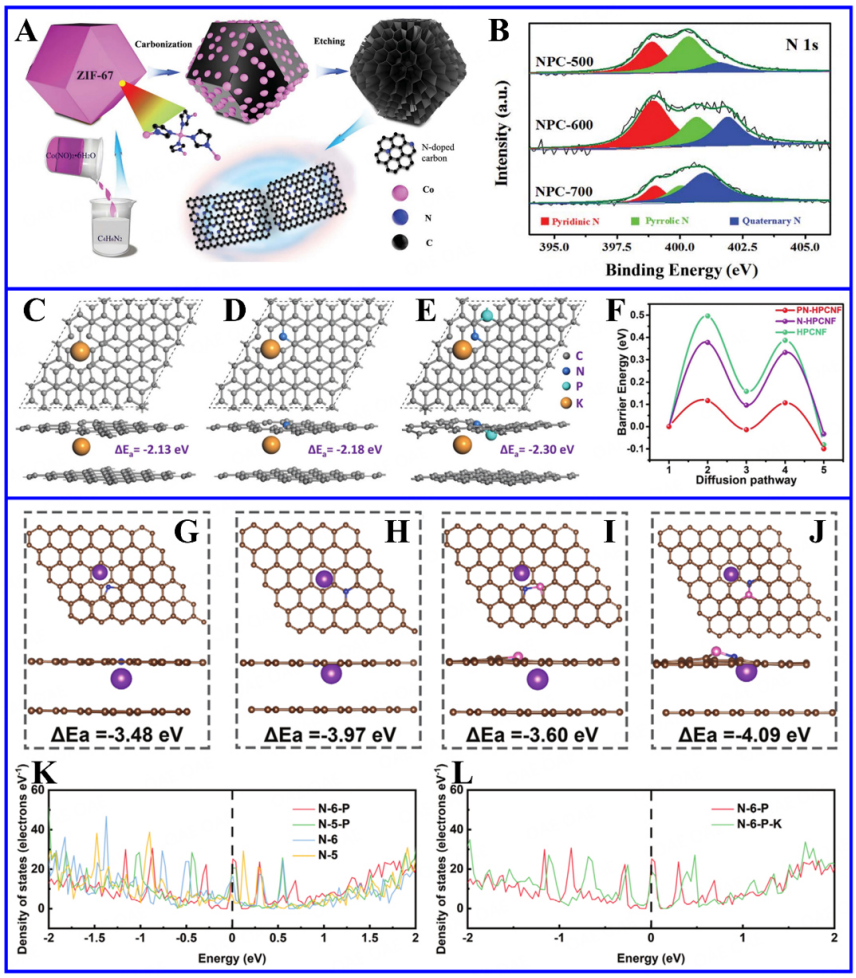

Figure 4. (A) Schematic of the synthesis process and (B) N 1s of NPC. This figure is quoted with permission from Li *et al.*[94]. The optimized model of a K ion adsorbed on (C) HPCNF, (D) N-HPCNF, (E) PN-HPCNF, and (F) corresponding barrier energy. This figure is quoted with permission from Hu *et al.*[99]. The optimized model of a K ion adsorbed on (G) N-5, (H) N-6, (I) N-5-P, and (J) N-6-P; (K and L) DOS before and after a K ion absorption. This figure is quoted with permission from Wu *et al.*[100].

pristine carbon, N-Q-doped carbon, N-5-doped carbon, and N-6-doped carbon were -0.38, 0.08, -1.62, and -3.26 eV, respectively, which indicated that N-5 and N-6 can improve the K ion adsorption ability. As the number of N-6 increased from 1 to 3, the adsorption energy was increased to -3.48 and -3.67 eV, respectively, indicating that a higher level of N-6 was conducive to improving potassium storage capacity.

Besides the N element, S is also often doped in carbon skeleton to enhance the potassium storage properties[96,97]. S doping can also increase the conductivity and active sites. Moreover, the larger atomic radius of S can extend layer spacing and reduce K ion diffusion barriers, thus forming more active sites. Zuo *et al.* adopted a Fe-based MOF (MIL-88A) as C and S precursor to prepare S-doped PC (S-MPC) through a multi-step synthesis strategy[98]. The as-synthesized S-MPC had a unique 3D flower-like nanostructure with abundant mesopores, which can promote K ion transport. Furthermore, S doping expanded the interlayer spacing and introduced rich electrochemical sites, which can enhance the storage capacity of K ions. First-principles calculations were used to corroborate the enhanced potassium storage enabled by S doping. The results indicated that the adsorption energies of K atoms on the S side and H side of S-doped carbon (-2.54 eV and -2.22 eV) were greater than that of pure carbon (-1.98 eV). Furthermore,

The K atom diffusion barriers of S-doped carbon on the S side and H side (0.62 eV and 0.49 eV) were lower than that of pure carbon (0.81 eV). Therefore, S doping can effectively enhance the adsorption and reduce the diffusion barrier of K ions.

Doping engineering (co-doping)

Compared with mono-doping, heteroatom co-doping can not only harvest the merits of respective heteroatoms but also incur interactions between different atoms, allowing for enhanced potassium storage performance. Moreover, the doping of one heteroatom can affect the content and species of another heteroatom dopant, which allows directional optimization of heteroatom co-doping. Therefore, the number of electrochemical sites and electronic structure of MOF-derived carbon can be adjusted through a co-doping strategy.

N/P co-doping is the most used strategy for MOF-derived carbon. Hu *et al.* prepared P/N co-doped carbon (named as PN-HPCNFs) from a mixed solution of ZIF-8, urea, polyacrylonitrile (PAN), and triphenylphosphine through electrospinning and subsequent high-temperature calcination[99]. The content of N-6 increased from 46.1% of N-HPCNFs to 55.2% of PN-HPCNFs, proving that additional P atoms can optimize the electronic structure and create more active sites, thus obtaining higher K ion storage capacity. P/N co-doping expanded the layer spacing to 0.41 nm, which is beneficial to alleviate the structural damage caused by K ion insertion/extraction, thus achieving an ultralong cycle life. In addition, the DFT calculation results showed that P/N co-doped carbon exhibited increased K ion adsorption energy and reduced diffusion barriers [Figure 4C-F], which further demonstrated the advantage of P/N co-doping in achieving elevated potassium storage. Similarly, Wu *et al.* prepared PNCNFs with ultrahigh N content (19.52 wt.%) and more N-6 active sites by calcining MET-6@PPh_3-PAN[100]. The DFT results revealed that the K ion was more easily adsorbed on N-6-P active sites [Figure 4G-J]. Moreover, the density of states (DOS) of the Fermi level at the N/P co-doped site was higher than that at the N-doped site, indicating that the introduction of additional P atoms increased the electronic conductivity [Figure 4K]. The comparable DOS values of the N-6-P site before and after K ion adsorption indicated the maintained high electronic conductivity during potassiation/depotassiation [Figure 4L]. Therefore, the introduction of P into the N-rich system can improve the K ion adsorption ability, facilitate electron transport, and render excellent reversible capacity and rate performance.

Zhu *et al.* prepared N/S co-doped carbon microspheres (NSCMs) through high-temperature calcination and acid washing of Zn-MOF-74 and rationalized the improved potassium storage performance of undoped carbon microspheres (CMs) by N/S co-doping through material characterization, kinetic analysis, and DFT calculations[101]. It was found that the intensity ratio of D-band to G-band (I_D/I_G), specific surface area ($m^2\ g^{-1}$), interlayer spacing (nm), and conductivity ($S\ cm^{-1}$) of NSCMs were 1.10, 1347.4, 0.408, and 8.74, respectively, all higher than those of CMs (1.05, 1014.8, 0.400, and 5.83), which can be attributed to N/S co-doping. The improved I_D/I_G and specific surface area can effectively create more defects for K ions adsorption, increasing potassium storage capacity. The expanded interlayer spacing and conductivity accelerate the K ions insertion/extraction and electrons transport, respectively, thereby improving the rate performance. The kinetics analysis showed that N/S co-doping can reduce the charge transfer resistance and increase the capacitive contribution, which promoted rapid mass transfer and led to enhanced rate performance. Moreover, the DFT calculations revealed that N/S co-doping can improve the adsorption capacity of CMs for K ions, which is beneficial for capturing and storing K ions. Therefore, N/S co-doping can optimize the physicochemical properties of carbon materials, thereby exhibiting enhanced potassium storage performance.

Besides N/P and N/S co-doping, N/O and O/F co-doped MOF-derived carbon was also explored. Yang *et al.* synthesized N/O co-doped PC with high N (7.06%) and O (7.90%) content by calcining and etching an Al-based MOF[93]. The additional O element can enhance wettability and increase effective contact area. Lu *et al.* prepared O/F dual-doped PC nanopolyhedra (OFPCN) as an anode for PIBs[102]. Through experimental results and DFT calculations, it was demonstrated that O/F co-doping can strengthen K ion adsorption without structural damage, which accounted for the excellent potassium storage properties.

Typical types of MOF-derived carbon composites

Differing from intercalation and adsorption reactions of carbon materials, metal compounds/alloying materials with conversion/alloying reactions show higher K ion storage capacity. Owing to inferior conductivity and huge volume change during charging/discharging, the practical application of metal compounds/alloying materials is limited by terrible rate and cycling performance. The combination of metal compounds/alloying materials and carbon can effectively improve conductivity and cycling stability. Moreover, rational structure design can relieve the volume expansion during cycling. Thanks to the abundant metal/heteroatom/carbon resources and controllable morphology, MOFs can be facilely converted into metal compound/carbon and alloying material/carbon composites. In addition, metal ions in pristine MOFs are evenly distributed, while the MOF-derived carbons prepared by high-temperature carbonization can well maintain the morphology of pristine MOFs, which ensures the uniform dispersion of generated metal compounds/alloying materials in the carbon matrix. Based on these advantages, abundant MOF-derived carbon composites, including metal oxide/carbon, metal phosphide/carbon, metal sulfide/carbon, and metal selenide/carbon composites, have been widely studied. Herein, we mainly discuss the application of these MOF-derived carbon composites in PIB anodes.

Metal oxide/carbon

Metal oxides have attracted extensive attention as PIB anodes on account of their excellent theoretical capacity and eco-friendliness[5]. The organic ligand of MOFs can not only anchor active metal oxides into the carbon skeleton but also alleviate the agglomeration of metal oxides during calcination, which is conducive to improving the cycle stability. For example, Hu *et al.* successfully prepared MoO_2@N-doped carbon nano-octahedron (MoO_2@NPC) from the MOF-based polyoxometalate (NENU-5)[103]. The MoO_2 nanoparticles (~10 nm) were evenly embedded in the carbon skeleton, which ensured the rapid K ion transfer between MoO_2 nanoparticles and carbon materials and reduced volume expansion during cycling. Moreover, DFT calculations showed the higher K ion adsorption energy of MoO_2@NPC than that of bare MoO_2 and NPC, suggesting the higher potassium storage capacity in MoO_2@NPC. Dubal *et al.* used Ti-based MOFs as a self-sacrificial template to synthesize a composite of ultrafine TiO_2 nanoparticles (1-3 nm) embedded in N-rich graphitic carbon (TiO_2@NGC) with hierarchical pores[104]. *Ex situ* characterization techniques revealed that the bare TiO_2 phase was converted into a mixed phase of Ti_7O_{13} and $K_2Ti_4O_9$ after the first potassiation/depotassiation, which further demonstrated the conversion-based potassium storage mechanism. As discussed earlier, the well-designed core-shell structure can shorten the K ion transport path and withstand the volume change during charging/discharging, thus facilitating K ion storage capacity. Wang *et al.* synthesized ZnO/$ZnFe_2O_4$/carbon with a core-double shell nanostructure, achieving excellent potassium storage properties[105]. Embedding metal oxides into the porous carbon skeleton of core-shell structures can promote K ions transfer and endure the volume expansion caused by the conversion reaction of metal oxides during cycling. As displayed in Figure 5A, a TiO_2/carbon composite wrapped by N/P/S co-doped carbon (TiO_2/C@NPSC) with a well-designed core-shell structure was synthesized by pyrolyzing a modified Ti-based MOF[106]. Consequently, the TiO_2/C@NPSC delivered excellent cycle stability (122.9 mAh g^{-1} at 1.0 A g^{-1} after 5,000 cycles) as a PIB anode [Figure 5B].

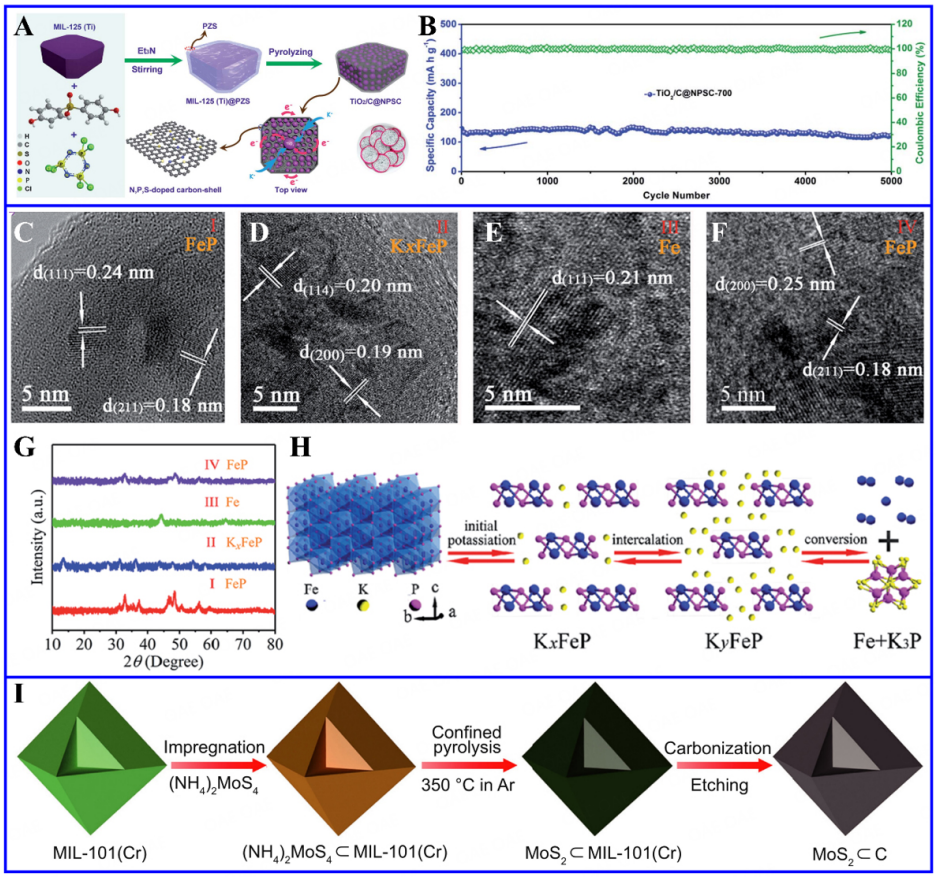

Figure 5. (A) Schematic of the synthesis process and (B) cyclic stability of TiO_2/C@NPSC. This figure is quoted with permission from Li *et al.*[106]. HRTEM images of 3DG/FeP after first discharge to (C) 2.0 V, (D) 0.9 V, (E) 0.01 V, and first charge to (F) 3.0 V; (G) XRD patterns of corresponding state; (H) Schematic of the K ion storage mechanism of 3DG/FeP. This figure is quoted with permission from Zhang *et al.*[107]. (I) Schematic of the synthesis process of MoS_2⊂C. This figure is quoted with permission from Hu *et al.*[118].

Metal phosphide/carbon

Metal phosphides are also widely used in PIBs owing to their high theoretical capacity and cost-effectiveness[5]. There are usually two strategies for synthesizing MOF-derived metal phosphide/carbon composites. One is that MOF precursors and P sources are calcined at high temperatures at the same time, and another is that MOF precursors are carbonized and then phosphatized by P sources. Following the first strategy, Zhang *et al.* successfully prepared a 3D graphene skeleton (3DG) and FeP hollow nanospheres (3DG/FeP) composite through a simple one-step thermal conversion[107]. The as-prepared 3DG/FeP possessed discrete FeP hollow nanospheres encapsulated by 3DG, resulting in excellent potassium storage properties. *Ex situ* high-resolution TEM (HRTEM) and X-ray diffraction (XRD) characterizations further revealed the intercalation and conversion-based potassium storage mechanism of 3DG/FeP, producing K_3P after the conversion reaction between FeP and K [Figure 5C-H]. Similarly, Das *et al.* prepared Co_2P nanoparticle encapsulated N-doped carbon (Co_2P@NCCs) via one-step carbonization-phosphorization of ZIF-67, which delivered a stable cycling performance as PIB anodes[108]. For another synthesis strategy, Jiang *et al.* synthesized N-doped carbon-limited CoP polyhedrons wrapped by rGO sheets (CoP/NC@rGO) for PIBs[109]. First, ZIF-67 and graphene oxide (GO) were mixed and carbonized to prepare intermediate Co/NC@rGO, which was then phosphatized to obtain CoP/NC@rGO. The as-synthesized composite possessed a ZIF-67-derived carbon matrix, encapsulating discrete CoP nanoparticles as the internal structure and highly conductive rGO as the external structure, which significantly improved conductivity and effectively

avoided CoP nanoparticle agglomeration. Thus, the CoP/NC@rGO anode achieved a satisfactory cycle performance.

Similar to metal oxides, embedding metal phosphides into the porous carbon skeleton of a well-designed core-shell structure can further enhance the potassium storage performance. Miao *et al.* electrospun a MOF (ZIF-8/ZIF-67) precursor and then synthesized a novel MOF-derived CoP/carbon composite with a 3D core-shell structure by a carbonization-oxidation-phosphorization strategy, showing excellent potassium storage properties[110]. Yi *et al.* synthesized ZIF-8@ZIF-67-derived NPC with confined CoP polyhedrons via a carbonization-phosphorization strategy[111]. First-principles calculations suggested that K ion was more likely to be located at the hollow site encompassed by three P atoms, with adsorption energy and diffusion barriers of about 0.79 eV and less than 0.06 eV, which was conducive to K ion diffusion on the CoP surface, enhancing the reaction kinetics. The DOS results showed that CoP/NC and CoP had no bandgap at the Fermi level, indicating good conductivity. These excellent characteristics ensured the good rate capability and cyclic stability of NC@CoP/NC.

Metal sulfide/carbon

Metal sulfides have become burgeoning candidate PIB anodes owing to their rich active sites, large interlayer spacing, and high theoretical capacity[5,112]. The non-etched MOF-derived carbon contains rich metal nanoparticles, which can form metal sulfide/carbon composites after further sulfidation. Miao *et al.* electrospun ZIF-8/ZIF-67 and then synthesized a novel MOF-derived CoS/carbon composite with 3D hierarchical structure units by a carbonization-oxidation-vulcanization strategy, showing excellent potassium storage performance[113]. In order to alleviate the agglomeration and collapse of MOFs, Zhou *et al.* introduced GO into the solution for the synthesis of Fe-MOF, which not only improved the dispersion of Fe-MOF but also increased the conductivity of the as-prepared FeS_2@C-rGO composites[114]. Similarly, Choi *et al.* used acid-treated carbon nanotube networks (ACNT) to provide a conductive framework and nucleation site for the *in-situ* growth of MOF-5[115]. The as-obtained ZnS nanoparticles with a size of ~15 nm were uniformly dispersed in MOF-5@ACNT-derived 3D-interconnected carbon networks after carbonization-vulcanization treatment, displaying ultradurable K ion storage.

MoS_2, a typical metal sulfide, has been widely studied in PIBs because its large interlayer spacing (0.62 nm) is conducive to the insertion/extraction of large-radius K ions[116-118]. Moreover, well-structured MoS_2/carbon composites can effectively overcome the drawbacks of poor conductivity and volume change of MoS_2 during cycling. Generally, MoS_2 can be coated on a carbon material surface via a hydrothermal method. Rui *et al.* used ZIF-67 as the polyhedron template and C/N sources to prepare ultrathin MoS_2 ornamented Co nanoparticle/carbon composite (ZIF-67-C@MoS_2)[116]. *In situ* growth of NCNTs and Co nanoparticles formed a cross-linking conductive network, which improved the conductivity and reduced the volume expansion of MoS_2 during cycling. Thus, the ZIF-67-C@MoS_2 anode delivered good potassium storage performance. Analogously, Jiang *et al.* coated MoS_2 nanosheets on ZIF-8-derived carbon, showing excellent potassium storage performance[117]. Different from coating MoS_2 on the carbon material surface, Hu *et al.* confined few-layer MoS_2 nanosheets (< 10 nm) to the interior of MOF-derived carbon (MoS_2⊂C) [Figure 5I][118]. The strong confinement effect of outer porous carbon inhibited the growth and aggregation of MoS_2, producing abundant edges and active sites for promoted K ions reaction kinetics.

Recently, emerging electrode materials with heterostructures have attracted considerable attention due to their stronger stability and higher capacity compared to the single component[119]. Furthermore, hetero-structured electrodes can combine the advantages of building blocks while offsetting the drawbacks of individual modules through synergistic effects. Li *et al.* successfully synthesized hetero-structured bimetallic

sulfides with VS_4 nanodots ornamented on CoS_2/N-doped carbon (CoS_2/NC@VS_4) and employed as PIB anodes[120]. The heterogeneous structure composed of CoS_2 and VS_4 was conducive to ensuring full contact with the electrolyte and shortening the diffusion length of K ions. Moreover, the N-doped carbon skeleton promoted electron transport and alleviated volume expansion during discharging/charging. Therefore, the CoS_2/NC@VS_4 anode achieved admirable ICE of 84.59% and high reversible capacity. Zhang *et al.* designed a Cu_9S_5/MoS_2 heterostructure wrapped in a GO matrix by a MOF-assisted strategy[121]. The *in-situ* thiophilic Cu^0 mesophase was evenly distributed in Mo^0/K_xS_y compounds, which is conducive to rapid charge transfer and anchoring of K_xS_y, thus improving the reversibility of the phase transition process. Additionally, the internal hollow structure and the external 3D conductive framework guarantee long cycling stability. As expected, the as-prepared composite delivered outstanding capacity and a long cycle lifespan.

Metal selenide/carbon

Compared with the metal-P and metal-S bonds, the metal-Se bond is easy to break due to the larger radius of Se than that of P and S, which is conducive to facilitated kinetics of conversion reaction. Thus, MOF-derived metal selenide/carbon composites are receiving increasing attention. Ma *et al.* implanted $Co_{0.85}Se$ particles in ZIF-67-derived N-doped carbon ($Co_{0.85}Se$@NC), which maintained the morphological characteristics of ZIF-67 with abundant small nanoparticles (20-38 nm)[122]. The $Co_{0.85}Se$@NC anode delivered excellent potassium storage performance. Since then, researchers prepared a variety of CoSe/carbon or ZnSe/carbon composites by calcining the ZIF-67 or ZIF-8 precursors with subsequent selenization, all of which delivered good potassium storage properties[123-125]. Different from the gasification selenization process of selenium powder, Kim *et al.* reported a simple solution-phase selenization method in which Co-Se bonds were formed by ion exchange between Se^{2-} in NaHSe solution and organic anions in ZIF-67[126]. Through crystallization and carbonization treatment, ultrafine $Co_{0.85}Se$ and N-doped carbon composite were successfully prepared. In order to improve the potassium storage performance of CoSe, Wang *et al. in situ* constructed ZIF-67-derived Co/CoSe Schottky heterojunction on the surface of hollow carbon nanospheres[127]. The close contact and strong electron coupling between Co and CoSe promoted the spontaneous electron flow from Co to CoSe at the contact interface, leading to charge redistribution. As a result, the enhanced lattice defects provide active sites for K^+ migration, thus improving the potassium storage performance. Similar to MoS_2, $MoSe_2$, with a unique 2D structure and broad interlayer spacing, is conducive to promoting the insertion/extraction of K ions but suffers from a huge volume change during cycling. Jiang *et al.* synthesized $MoSe_2$ nanosheets on the NPC polyhedron through annealing ZIF-8 and a subsequent solvothermal strategy[128]. Thanks to the synergistic effects between $MoSe_2$ and carbon, the composite delivered high capacity and excellent rate performance.

Rational structural design of MOF-derived metal selenide/carbon composites is conducive to further improving K ion storage performance. Na *et al.* synthesized ultrasmall ZnSe nanocrystals embedded in carbon nanofibers (ZnSe@PCNF) by electrospinning ZIF-8 and a subsequent carbonization-selenization strategy, which delivered good potassium storage properties[129]. Wang *et al.* synthesized ZIF-8@ZIF-67-derived carbon nanotubes confining metal Se (Co-Se@CNNCP) with a 3D core-shell structure by a carbonization-selenization strategy[130]. In addition, wrapping metal selenides in the interior of the hollow porous carbon is an effective strategy to improve electronic conductivity and alleviate volume changes during cycling. Liu *et al.* adopted the unique microporous openings and mesoporous cages of a Fe-based MOF to well constrain metal selenide and prepare FeSe@C with a mesoporous structure, which exhibited outstanding potassium storage properties[131]. Yang *et al.* reported a vacuum-assisted method to prepare carbon-coated $CoSe_2$ nanoparticles confined in the interior of hollow mesoporous carbon nanospheres ($CoSe_2$@NC/HMCS)[132]. Owing to the "double confinement" of the carbon skeleton derived from ZIF-67 and HMCS, the $CoSe_2$ nanoparticles were confined in the interior of HMCS, ensuring ultrahigh reversible

capacity and outstanding rate capability in $CoSe_2$@NC/HMCS anode. Ruan *et al.* also constructed a "double-carbon-confined" framework (ZnSe@i-NMC@o-rGO), and ZnSe was confined by internal ZIF-8-derived microporous carbon and further wrapped in external rGO sheets [Figure 6A][133]. The stress distribution of ZnSe structures in three models (ZnSe, ZnSe@i-NMC, and ZnSe@i-NMC@o-rGO) during potassiation was studied via a finite element method [Figure 6B], revealing the smallest axial stress and maximum stress of ZnSe particle in ZnSe@i-NMC@o-rGO and indicating the superior mechanical stability of the double-carbon constrained structure and outstanding cyclic stability for PIB anode.

To enhance the potassium storage performance, bimetallic selenides were prepared as PIB anode materials. Oh *et al.* successfully synthesized novel MC-Se@NC with 1D hybrid nanostructures by carbonization-selenization of ZIF-67-coated MoO_3 nanorods, which contained a $MoSe_2$ core and a $CoSe_2$/N-doped carbon shell[134]. Owing to the abundant active sites provided by the synergistic $MoSe_2$ and $CoSe_2$, enhanced electronic conductivity, and alleviated volume expansion during cycling ensured by N-doped carbon coatings, the MC-Se@NC delivered great potassium storage properties. Zhou *et al.* synthesized carbon anchoring Zn-Mn binary selenides (ZMS@FC) as PIB anodes[135]. With the aid of structural control reagents, Zn and Mn ions were cross-linked with trimesic acid and self-assembled into flower-like MOFs (Zn-Mn-BTC) by a solvothermal method. Subsequently, the flower-like ZMS@FC was obtained by calcining Zn-Mn-BTC mixed with selenium powder. The 2D porous petal layered structure not only improved the electrode surface wettability and electron transfer efficiency but also effectively limited the volume change, which played a key role in enhancing rate performance and stabilizing long cycle life. Through *ex situ* XRD and TEM characterization, a highly reversible conversion-based potassium storage mechanism was confirmed in ZMS@FC.

Alloying material/carbon

The emerging alloying-type materials, including Sn, Sb, Bi, and P, have been considered as promising PIB anode materials due to their high theoretical capacity, appropriate working potential, and attractive safety. Notwithstanding, serious volume damage during potassiation/depotassiation is still a key challenge, resulting in inferior cycle lifespan and severe capacity attenuation. The strategies of nanostructure engineering and carbon decoration could effectively reduce the volume dilation of alloying-type anodes. Nanoparticles can significantly reduce the mechanical stress during potassiation, thereby alleviating the pulverization. In addition, the introduction of carbon materials with strong mechanical elasticity, high conductivity, and stable structure into metal nanoparticles can improve conductivity and buffer volume dilation or agglomeration. Therefore, MOF-derived alloying-based electrodes show great application prospects in PIBs. Yan *et al.* synthesized highly dispersed zinc particles in carbon networks (ZNP/C) via calcining ZIF-8 precursors[136]. The as-prepared ZNP/C delivered a satisfactory capacity due to the unique structure composed of highly dispersed zinc nanoparticles and conductive carbon networks, which inhibited the volume change in the alloying/dealloying (Zn↔KxZn) process.

Metal Bi has been widely used in PIBs owing to its relatively high theoretical capacity (385.0 mAh g^{-1}; Bi↔KxBi), large lattice spacing, high electronic conductivity, and low cost[137]. Su *et al.* synthesized ultrathin carbon film@carbon nanorods@Bi nanoparticle (UCF@CNs@BiNs) composites for PIB anodes [Figure 6C][138]. The UCF@CNs@BiNs possessed a rod-shaped structure, which was completely wrapped by a 6 nm thick carbon film and abundant Bi nanoparticles evenly distributed in a carbon nanorod framework. The UCF@CN matrix enabled the SEI formation on carbon film instead of Bi nanoparticles, thus mitigating the decomposition of active materials and achieving stable cycling performance [Figure 6D and E]. Sun *et al.* successfully encapsulated Bi nanoparticles into a 3D foam-like carbon nanocage framework (Bi@N-CNCs) by annealing 2D Bi-based MOFs[139]. Thanks to the unique structure and composition, the as-

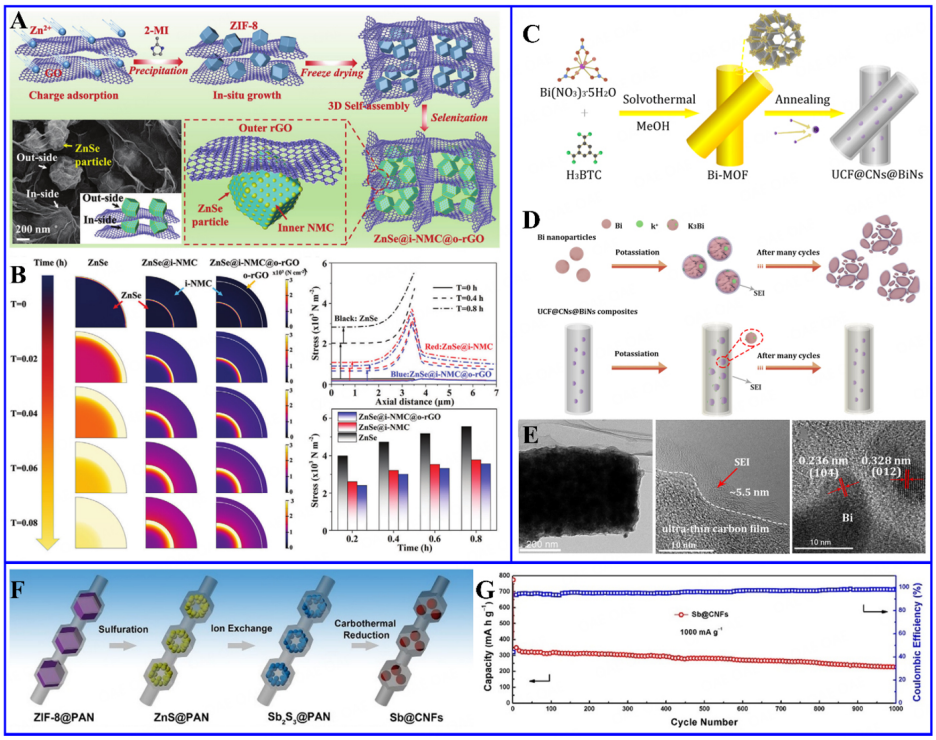

Figure 6. (A) Schematic of the synthesis process and corresponding SEM image of ZnSe@i-NCM@o-rGO; (B)The stress distribution in ZnSe, ZnSe@i-NMC, and ZnSe@i-NMC@o-rGO at different stages of K ion intercalation reaction and corresponding axial stress distribution and the maximum stress. This figure is quoted with permission from Ruan *et al.*[133]. (C) Schematic of the synthesis process of UCF@CNs@BiNs; (D) Schematics of Bi and UCF@CNs@BiNs electrode during the cycle; (E) TEM and HRTEM images of UCF@CNs@BiNs after many cycles. This figure is quoted with permission from Su *et al.*[138]. (F) Schematic of the synthesis process and (G) cycle performance of Sb@CNFs. This figure is quoted with permission from Huang *et al.*[142].

prepared sample achieved excellent K ions storage properties. In addition, Tong *et al.* prepared metastable Bi:Co or Bi:Fe alloying materials and carbon composites (Bi:Co@C or Bi:Fe@C) by annealing Bi-Co-MOF or Bi-Fe-MOF precursors, all of which exhibited excellent potassium storage performance[140].

Metal Sb is another promising alloying-type anode material for PIBs because of its high theoretical capacity (660.0 mAh g^{-1}; Sb↔KxSb), low alloying reaction potential, and great conductivity[137]. Cheng *et al.* successfully embedded uniform Sb nanoparticles (~19 nm) into porous carbon (Sb-NPs@PC) by simple annealing treatment of Sb-MOF precursors, which delivered ultrahigh reversible capacity and excellent rate performance[141]. Huang *et al.* successfully designed a hybrid yolk-shell structure constituted of Sb nanoparticles as yolk and carbon nanofibers as shell (Sb@CNFs) through a MOF electrospinning coupled with confined ion-exchange strategy followed by subsequent thermal reduction [Figure 6F][142]. Consequently, the Sb@CNFs maintained an excellent capacity of 227 mAh g^{-1} after 1,000 cycles at 1.0 A g^{-1} with CE of approximately 100% [Figure 6G].

In addition to metal-based alloying materials, P-based materials have attracted extensive attention in PIBs because of their safety, environmentally friendly, low cost, and ultrahigh theoretical capacity (2,956.0 mAh g^{-1}; P↔K_3P)[143]. Sui *et al.* embedded red P into carbon nanorods derived from Zn-MOF (P@ZCRods)[144]. By adjusting the size and P content, the optimized P@ZCRods achieved superior ICE of 78.5% and a remarkable reversible capacity of 595.8 mAh g^{-1}. Similarly, Liang *et al.* prepared carbon superstructure by calcining Al-based MOFs, which were further used as a substrate to confine red P

effectively[145]. As a result, the as-prepared sample exhibited satisfactory potassium storage properties.

Recently, electrode materials with conversion-alloying reactions have received attention as they exhibit higher capacity than single alloying materials through dual storage mechanisms[146]. Chen *et al.* utilized the excellent structure of Bi-based MOFs and a carbonization-selenization technique to uniformly embed Bi/Bi_3Se_4 hybrid nanoparticles into hollow porous carbon nanorods[147]. The external hollow porous carbon framework derived from Bi-MOF manifested structural integrity, which not only prevented the aggregation of Bi-based active nanoparticles but also provided rich ion/electron transfer channels. In addition, the composite possessed rich C-O-Bi bonds, indicating a close connection between Bi/Bi_3Se_4 nanoparticles and the carbon matrix, which further enhanced the stability of Bi-based active particles. As a result, the assembled half-cell showed an ultrahigh rate capacity of 307.5 mAh g^{-1} at 20.0 A g^{-1}. Zhang *et al.* embedded Bi_2O_3 nanomaterials in a carbon framework by carbonization and further oxidation of Bi-MOF precursors[148]. The Bi_2O_3@C anode achieved a high reversible capacity via a conversion-alloying reaction ($Bi_2O_3 \leftrightarrow Bi \leftrightarrow K_3Bi$). Tong *et al.* designed Bi/Bi_2O_3-C with heterostructure for PIB anodes via annealing an accordion-like structure of Bi-based MOFs[149].

Summary

We summarized the electrochemical performance of MOF-derived carbon and its composites as PIB anode materials, as shown in Table 1. Through rational structural design and doping engineering, MOF-derived carbon exhibit enhanced reversible capacity, favorable rate capability, and cyclic stability. However, the ICE values are usually less than 50% because of their large specific surface area. In general, K ions in PIB full cells come from commercial cathodes, but exorbitant consumption of K ions will restrain the industry application of these anode materials. Therefore, many efforts are still needed to improve the ICE without sacrificing the merits of MOF-derived carbon anodes. Encouragingly, MOF-derived carbon composites possess higher ICE values (mainly > 50%) than MOF-derived carbon; meanwhile, their rate performance and cycle life are better than those of bare metal compounds and alloying materials. However, the cyclic stability of MOF-derived carbon composites (mainly < 1,000 cycles) is inferior to that of MOF-derived carbon. At present, the design of MOF-derived carbon composites mainly focuses on structural optimization and composition diversification but ignores the carbon content tuning, which also affects the cycle performance. Therefore, there are still great challenges in improving the overall electrochemical properties of MOF-derived carbon and its composites.

ADVANCED CHARACTERIZATION FOR PIB ANODES

As mentioned above, the application of MOF-derived carbon and its composites in PIBs is still at its early stage, and the performance needs to be further enhanced. Therefore, a more in-depth exploration of working mechanisms is needed to better optimize potassium storage performance. Although plentiful *ex situ* characterization methods have been widely used in the study of potassium storage mechanisms and some achievements have been made, these technologies cannot avoid exposure of electrodes to air during battery disassembly, electrode cleaning, and transfer[48]. Therefore, it is necessary to develop advanced characterization techniques to monitor the electrode material during charging/discharging in real time to ensure the accuracy of the results. *In situ* characterization technologies, including *in situ* Raman, *in situ* XRD, *in situ* TEM, and so on, have been widely employed in the mechanism research of alkaline ion batteries and supercapacitors[150,151]. For PIBs, these advanced techniques can continuously monitor the SEI film formation, ion transport process, and electrode structure evolution of PIBs during the cycle, which is conducive to a deeper understanding of the reaction process and potassium storage mechanism under actual operating conditions. In this section, we mainly summarized the application of *in situ* characterization technologies in PIB anodes.

Table 1. The electrochemical performance of MOF-derived carbon and its composites for PIBs

Anode materials	MOF precursors (Organic ligands)	Electrolyte	ICE (%)	Rate capability (mAh g^{-1})	Cycling stability (mAh g^{-1})	Ref.
NCNTs	ZIF-67 (2-methylimidazole)	0.8 M KPF_6 in EC/DEC (v/v = 1:1)	24.5	293.1 at 0.05 A g^{-1} 131.0 at 2.0 A g^{-1}	102.0 at 2.0 A g^{-1} after 500 cycles	[79]
AC@GC	ZnCo-MOF (2-methylimidazole)	0.7 M KPF_6 in EC/DEC (v/v = 1:1)	15.7	460.0 at 0.1 A g^{-1} 120.0 at 5.0 A g^{-1}	192.0 at 1.0 A g^{-1} after 5,200 cycles	[80]
HCONs	Co-MOF (Hexamine)	0.8 M KPF_6 in EC/DEC (v/v = 1:1)	26.0	311.0 at 0.1 A g^{-1} 136.0 at 5.0 A g^{-1}	132.0 at 2.0 A g^{-1} after 5,000 cycles	[81]
C_{700}	Cu-MOF (H_2BDC)	M KFSI in EC/DEC (v/v = 1:1)	40.7	283.7 at 0.1 A g^{-1} 184.5 at 2.0 A g^{-1}	170.8 at 1.0 A g^{-1} after 500 cycles	[83]
Carbon networks	ZIF-67 (2-methylimidazole)	0.8 M KPF_6 in EC/DEC (v/v = 1:1)	45.0	270.0 at 0.05 A g^{-1} 100.0 at 2.0 A g^{-1}	202.5 at 0.05 A g^{-1} after 500 cycles	[84]
NSC	S-ZIF-67 (2-methylimidazole)	0.8 M KPF_6 in EC/DEC (v/v = 1:1)	38.0	296.2 at 0.2 A g^{-1} 151.6 at 2.0 A g^{-1}	180.5 at 0.5 A g^{-1} after 1,000 cycles	[85]
ZnCo-MOF-74 @ZIF-8-C	ZnCo-MOF-74 (DHBDC)	0.8 M KPF_6 in EC/DEC (v/v = 1:1)	46.2	523.2 at 0.05 A g^{-1} 138.3 at 3.0 A g^{-1}	175.0 at 1.0 A g^{-1} after 2,000 cycles	[87]
NCS	Al-MOF (2-amino-terephthalic acid)	1.0 M KFSI in EC/DEC (v/v = 1:1)	29.0	305.0 at 0.1 A g^{-1} 162.0 at 6.0 A g^{-1}	162.0 at 6.0 A g^{-1} after 500 cycles	[88]
SCNC	ZIF-8 (2-methylimidazole)	1.0 M KFSI in DME	38.5	341.7 at 0.1 A g^{-1} 188.2 at 2.0 A g^{-1}	176.4 at 2.0 A g^{-1} after 1,800 cycles	[89]
N-HPC	3DOM-ZIF-8 (2-methylimidazole)	0.7 M KPF_6 in EC/DEC (v/v = 1:1)	15.0	345.0 at 0.1 A g^{-1} 94.0 at 10.0 A g^{-1}	157.0 at 2.0 A g^{-1} after 12,000 cycles	[90]
NMCP@rGO	ZIF-8 (2-methylimidazole)	1.0 M KPF_6 in EC/DEC (v/v = 1:1)	50.8	351.0 at 0.05 A g^{-1} 194.0 at 5.0 A g^{-1}	151.4 at 5.0 A g^{-1} after 6,000 cycles	[91]
NPC	ZIF-67 (2-methylimidazole)	0.8 M KPF_6 in EC/DEC (v/v = 1:1)	30.0	359.6 at 0.2 A g^{-1} 186.2 at 2.0 A g^{-1}	231.6 at 0.5 A g^{-1} after 2,000 cycles	[94]
NPCF	MET-6 (1H-1,2,3-triazole)	0.8 M KFSI in EC/DEC (v/v = 1:1)	21.0	409.0 at 0.1 A g^{-1} 105.0 at 20.0 A g^{-1}	258.9 at 1.0 A g^{-1} after 2,000 cycles	[95]
S-MPC	MIL-88A (Fumaric acid)	0.8 M KPF_6 in EC/DEC (v/v = 1:1)	41.3	358.4 at 0.05 A g^{-1} 192.6 at 2.0 A g^{-1}	206.3 at 1.0 A g^{-1} after 700 cycles	[98]
PN-HPCNF	ZIF-8 (2-methylimidazole)	1.0 M KFSI in DEGDME	78.9	327.0 at 0.1 A g^{-1} 194.0 at 10.0 A g^{-1}	226.0 at 2.0 A g^{-1} after 10,000 cycles	[99]
PNCNFs	MET-6 (1H-1,2,3-triazole)	1.0 M KFSI in EC/DEC (v/v = 1:1)	48.0	407.5 at 0.1 A g^{-1} 244.4 at 8.0 A g^{-1}	294.6 at 2.0 A g^{-1} after 3,250 cycles	[100]
NOHPHC	NH_2-MIL-101 (NH_2-H_2BDC)	0.8 M KPF_6 in EC/DEC (v/v = 1:1)	25.0	365 at 0.025 A g^{-1} 118.0 at 3.0 A g^{-1}	130.0 at 1.05 A g^{-1} after 1,100 cycles	[93]
NSCM	Zn-MOF-74 (DHBDC)	1.0 M KPF_6 in EC/DEC (v/v = 1:1)	36.6	435.7 at 0.1 A g^{-1} 133.5 at 10.0 A g^{-1}	97.7 at 10.0 A g^{-1} after 2,500 cycles	[101]
OFPCN	UIO-66	0.8 M KFSI in EC/DEC	27.0	481.0 at 0.05 A g^{-1}	111.0 at 10.0 A g^{-1} after 5,000 cycles	[102]

	(H_2BDC)	(v/v = 1:1)		78.0 at 20.0 A g^{-1}	
MoO_2@NPC	NENU-5 (Trimesic acid)	1.0 M KFSI in DME	31.5	332.8 at 0.05 A g^{-1} 64.0 at 5.0 A g^{-1}	107.6 at 0.5 A g^{-1} after 500 cycles [103]
TiO_2@NGC	NH_2-MIL-125 (NH_2-H_2BDC)	1.0 M KPF_6 in EC/DMC (v/v = 1:1)	44.0	228.0 at 0.05 A g^{-1} 114.0 at 1.0 A g^{-1}	126.0 at 0.5 A g^{-1} after 2,000 cycles [104]
ZnO/$ZnFe_2O_4$	$Zn_3[Fe(CN)_6]_2$ ($K_3Fe(CN)_6$)	1.0 M KFSI in EC/DEC (v/v = 1:1)	52.0	239.0 at 0.1 A g^{-1} 31.0 at 5.0 A g^{-1}	60.0 at 1.0 A g^{-1} after 2,000 cycles [105]
TiO_2/C@NPSC	MIL-125 (Hexachlorocyclophosphazene and 4,4′-sulfonyldiphenol)	0.8 M KPF_6 in EC/DEC (v/v = 1:1)	46.9	299.4 at 0.05 A g^{-1} 112.1 at 2.0 A g^{-1}	122.9 at 1.0 A g^{-1} after 5,000 cycles [106]
3DG/FeP	3DG/PB ($Na_4Fe(CN)_6$)	1.0 M KPF_6 in EC/DEC (v/v = 1:1)	31.0	332.0 at 0.1 A g^{-1} 101.0 at 5.0 A g^{-1}	127.0 at 2.0 A g^{-1} after 2,000 cycles [107]
Co_2P@NCCs	ZIF-67 (2-methylimidazole)	0.8 M KPF_6 in EC/DEC/PC (v/v/v = 2:1:2)	42.0	196.0 at 0.1 A g^{-1} 91.0 at 2.0 A g^{-1}	125.0 at 0.5 A g^{-1} after 1,000 cycles [108]
CoP/NC@rGO	ZIF-67 (2-methylimidazole)	0.8 M KPF_6 in EC/DEC (v/v = 1:1)	42.3	360.0 at 0.1 A g^{-1} 155.0 at 2.0 A g^{-1}	177.0 at 1.0 A g^{-1} after 2,800 cycles [109]
AC@CoP/NCNTs/CNFs	ZIF-8/ZIF-67 (2-methylimidazole)	0.8 M KPF_6 in EC/DEC (v/v = 1:1) with 5.0% FEC	53.2	480.0 at 0.1 A g^{-1} 292.0 at 3.2 A g^{-1}	250.0 at 0.8 A g^{-1} after 1,000 cycles [110]
NC@CoP/NC	ZIF-8@ZIF-67 (2-methylimidazole)	0.8 M KPF_6 in EC/DEC (v/v = 1:1)	26.9	325.0 at 0.1 A g^{-1} 200.0 at 2.0 A g^{-1}	110.0 at 0.5 A g^{-1} after 800 cycles [111]
AC@CoS/NCNTs/CoS@CNFs	ZIF-8/ZIF-67 (2-methylimidazole)	0.8 M KPF_6 in EC/DEC (v/v = 1:1)	57.6	486.7 at 0.1 A g^{-1} 133.1 at 6.4 A g^{-1}	130.0 at 3.2 A g^{-1} after 600 cycles [113]
FeS_2@C-rGO	MIL-100 (Trimesic acids)	1.0 M KFSI in DME	63.0	526.0 at 0.1 A g^{-1} 301.0 at 5.0 A g^{-1}	171.0 at 2.0 A g^{-1} after 500 cycles [114]
ZnS/C@CNT	MOF-5 (H_2BDC)	1.0 M KFSI in EC/DMC (v/v = 1:1)	48.0	440.0 at 0.05 A g^{-1} 141.0 at 3.0 A g^{-1}	310.0 at 0.5 A g^{-1} after 1,000 cycles [115]
ZIF-67-C@MoS_2	ZIF-67 (2-methylimidazole)	0.8 M KPF_6 in EC/DEC (v/v = 1:1)	66.5	261.5 at 0.1 A g^{-1} 26.4 at 5.0 A g^{-1}	199.8 at 0.1 A g^{-1} after 50 cycles [116]
PCP@MoS_2	ZIF-8 (2-methylimidazole)	3.0 M KFSI in EC/DMC (v/v = 1:1)	69.0	376.0 at 0.1 A g^{-1} 228.0 at 2.0 A g^{-1}	100.0 at 0.5 A g^{-1} after 1,000 cycles [117]
MoS_2⊂C	MIL-101 (H_2BDC)	0.8 M KPF_6 in EC/DMC (v/v = 1:1)	49.6	341.0 at 0.5 A g^{-1} 94.0 at 10.0 A g^{-1}	200.0 at 2.0 A g^{-1} after 150 cycles [118]
CoS_2/NC@VS_4	ZIF-67 (2-methylimidazole)	1.0 M KPF_6 in DME	84.6	408.66 at 0.1 A g^{-1} 232.03 at 5.0 A g^{-1}	291.54 at 1.0 A g^{-1} after 430 cycles [120]
CMS/C	NENU-5 (Trimesic acids)	3.0 M KFSI in DEGDME	37.8	325.1 at 0.1 A g^{-1} 100.2 at 10.0 A g^{-1}	155.0 at 1.0 A g^{-1} after 1,000 cycles [121]
$Co_{0.85}Se$@NC	ZIF-67 (2-methylimidazole)	0.8 M KPF_6 in EC/DEC (v/v = 1:1) with 3.0 wt% FEC	57.9	319.9 at 0.05 A g^{-1} 110.7 at 2.0 A g^{-1}	114.7 at 1.0 A g^{-1} after 250 cycles [122]

ZnSe NP@NHC	ZIF-8 (2-methylimidazole)	5.0 M KTFSI in DEGDME with 1.0 wt% KNO_3	47.7	244.4 at 0.025 A g^{-1} 87.9 at 0.2 A g^{-1}	111.0 at 0.2 A g^{-1} after 1,600 cycles	[123]
ZnSe@NDPC	ZIF-8 (2-methylimidazole)	0.8 M KPF_6 in EC/DEC (v/v = 1:1)	41.1	297.3 at 0.5 A g^{-1} 52.8 at 5 A g^{-1}	109.1 at 0.5 A g^{-1} after 500 cycles	[124]
CoSe@NC	ZIF-67 (2-methylimidazole)	3.0 M KFSI in DME	70.0	411.8 at 0.05 A g^{-1} 365.9 at 2.0 A g^{-1}	299.0 at 2.0 A g^{-1} after 500 cycles	[125]
sol-CoSe@NC	ZIF-67 (2-methylimidazole)	1.0 M KFSI in EC/DEC (v/v = 1:1)	47.0	370.3 at 0.1 A g^{-1} 202.9 at 4.0 A g^{-1}	201.7 at 0.5 A g^{-1} after 200 cycles	[126]
CoSe/HCS	ZIF-67 (2-methylimidazole)	1.0 M KFSI in EC/DEC (v/v = 1:1)	66.7	900.0 at 0.2 A g^{-1} 120.0 at 5.0 A g^{-1}	145.9 at 10.0 A g^{-1} after 3,000 cycles	[127]
NPCP@$MoSe_2$	ZIF-8 (2-methylimidazole)	3.0 M KFSI in EC/DMC (v/v = 1:1)	39.0	322.0 at 0.1 A g^{-1} 134.0 at 5.0 A g^{-1}	128.0 at 0.5 A g^{-1} after 800 cycles	[128]
ZnSe@PCNF	ZIF-8 (2-methylimidazole)	3.0 M KFSI in DEGDME	66.0	361.0 at 0.1 A g^{-1} 158.0 at 2.0 A g^{-1}	270.0 at 0.5 A g^{-1} after 1,000 cycles	[129]
Co-Se@CNNCP	ZIF-8/ZIF-67 (2-methylimidazole)	3.0 M KFSI in EC/DMC (v/v = 1:1)	33.0	342.0 at 0.1 A g^{-1} 280.0 at 5.0 A g^{-1}	253.0 at 0.5 A g^{-1} after 200 cycles	[130]
FeSe@C	MIL-100 (Trimesic acids)	3.0 M KFSI in EC/DEC (v/v = 1:1)	67.6	420.0 at 0.1 A g^{-1} 254.0 at 2.0 A g^{-1}	310.0 at 0.5 A g^{-1} after 1,000 cycles	[131]
$CoSe_2$@NC/HMCS	ZIF-67 (2-methylimidazole)	1.0 M KFSI in EC/DEC (v/v = 1:1)	66.0	394.0 at 0.1 A g^{-1} 263.0 at 2.0 A g^{-1}	442.0 at 0.1 A g^{-1} after 120 cycles	[132]
ZnSe@i-NMC @o-rGO	ZIF-8@GO (2-methylimidazole)	1.0 M KPF_6 in DME	49.6	594.0 at 0.05 A g^{-1} 364.0 at 2.0 A g^{-1}	233.4 at 2.0 A g^{-1} after 1,500 cycles	[133]
MC-Se@NC	MoO_3/ZIF-67 (2-methylimidazole)	3.0 M KFSI in DEGDME	78.0	290.0 at 0.2 A g^{-1} 190.0 at 2.0 A g^{-1}	327.0 at 0.5 A g^{-1} after 150 cycles	[134]
ZMS@FC	Zn-Mn-MOF (Trimesic acids)	1.0 M KPF_6 in EC/DEC (v/v = 1:1)	84.0	328.6 at 0.1 A g^{-1} 156.9 at 5.0 A g^{-1}	227.0 at 2.0 A g^{-1} after 500 cycles	[135]
ZNP/C	ZIF-8 (2-methylimidazole)	0.8 M KPF_6 in EC/DMC (v/v = 1:1)	58.5	277.0 at 0.1 A g^{-1} 46.0 at 2.0 A g^{-1}	145.0 at 0.5 A g^{-1} after 300 cycles	[136]
UCF@CNs@BiNs	Bi-MOF (Trimesic acids)	3.0 M KFSI in DME	75.0	430.0 at 0.1 A g^{-1} 140.0 at 1.0 A g^{-1}	90.5 at 1.0 A g^{-1} after 700 cycles	[138]
Bi@N-CNCs	Bi-MOF (Trimesic acids)	1.0 M KPF_6 in DME	78.0	334.3 at 0.5 A g^{-1} 235.5 at 10.0 A g^{-1}	224.0 at 5.0 A g^{-1} after 1,200 cycles	[139]
$Bi_{0.83}Fe_{0.17}$@C	Bi-Fe-MOF (Trimesic acids)	1.0 M KPF_6 in DME	55.0	354.0 at 0.2 A g^{-1} 253.0 at 20.0 A g^{-1}	279.0 at 2.0 A g^{-1} after 975 cycles	[140]
Sb-NPs@PC	Sb-MOF (Terephthalic acid)	4.0 M KFSI in EMC	73.5	551.0 at 0.05 A g^{-1} 160.0 at 2.0 A g^{-1}	497.0 at 0.1 A g^{-1} after 100 cycles	[141]
Sb@CNFs	ZIF-8@PAN (1- and 2-methylimidazole)	2.0 M KFSI in DME	47.0	448.0 at 0.1 A g^{-1} 121.0 at 2.0 A g^{-1}	227.0 at 1.0 A g^{-1} after 1,000 cycles	[142]
P@ZCRods	Zn-MOF-74 (2,5-dihydroxyterephtalic acid)	2.4 M KFSI in EC/EMC (v/v = 1:1)	78.5	579.8 at 0.05 A g^{-1} 187.5 at 5.0 A g^{-1}	150.7 at 2.5 A g^{-1} after 400 cycles	[144]

P@NCS	Al-MOF (2-amino-terephthalic acid)	1.0 M KFSI in EC/DEC (v/v = 1:1)	76.0	561.0 at 0.2 A g^{-1} 238.0 at 8.0 A g^{-1}	271.0 at 1.0 A g^{-1} after 500 cycles	[145]
Bi/Bi_3Se_4@CNR	Bi-MOF (Trimesic acids)	1.0 M KPF_6 in DME	74.0	393.0 at 0.5 A g^{-1} 307.5 at 20.0 A g^{-1}	254.8 at 5.0 A g^{-1} after 2,000 cycles	[147]
Bi_2O_3@C	Bi-MOF (Trimesic acids)	1.0 M KFSI in EC/DEC (v/v = 1:1)	55.0	350.0 at 0.1 A g^{-1} 188.0 at 1.0 A g^{-1}	314.0 at 0.05 A g^{-1} after 100 cycles	[148]
Bi/Bi_2O_3-C	Bi-MOF (Trimesic acids)	5.0 M KFSI in DME	71.0	426.0 at 0.05 A g^{-1} 82.7 at 1.0 A g^{-1}	81.9 at 0.5 A g^{-1} after 900 cycles	[149]

In situ Raman

Raman spectroscopy is a non-destructive analysis method applied to solids, solutions, pure substances, and mixtures, which effectively provides detailed information, including phase, morphology, chemical structure, crystallinity, and graphitization degree. Therefore, *in situ* Raman can realize dynamic monitoring of electrode materials during discharging/charging. Zhou *et al.* investigated the potassiation/depotassiation mechanism during cyclic voltammetry scans of N-HPC by *in situ* Raman[90]. Figure 7A shows the schematic of *in situ* Raman testing. There are three obvious phenomena during the potassiation process [Figure 7B]. First, the G peak gradually shifted from 1,595 to 1,558 cm^{-1} when discharged from 3.01 to 0.30 V, which can be attributed to the increased steric hindrance and electron density with K ion insertion, resulting in the stretching of C-C bonds in the plane. This expansion produces biaxial strain, causing the red shift of the G peak. Second, no obvious symmetrical G peaks can be observed at 0.01 V, which can be attributed to the interference between the metal-like behavior of the intercalation compound and the resonance phonon scattering process, leading to decreased intensity of the G peak. Third, the value of I_D/I_G gradually decreased, indicating that K ions filled the defects of the material and increased graphitization. During the subsequent depotassiation process [Figure 7C], *in situ* Raman spectroscopy displayed the opposite changes. The G peak was blue-shifted when charged from 0.01 V to 3.00 V. The I_D/I_G value and G peak intensity were also restored to the initial state, indicating high reversibility. Thus, the working mechanism in N-HPC was speculated to be K ions adsorption on surface-active sites and filling in nanopores. Liang *et al.* also explored the working mechanism of NCS by *in situ* Raman testing [Figure 7D-F][88]. The G peak shifted from 1,572 to 1,524 cm^{-1} when discharged to 0.01 V, which might be due to the expansion of the C-C bond in the plane caused by the increased steric hindrance and electron density. After charging to 2.8 V, the G peak shifted back to 1,572 cm^{-1}, demonstrating a highly reversible discharging/charging process. In addition, the value of I_D/I_G decreased during potassiation, which might be due to the filling of K ions into the defective N-doped micropores of NCS.

In addition to MOF-derived carbon materials, the *in situ* Raman technique has also played an important role in revealing the potassium storage mechanism of MOF-derived composite materials. Recently, Jiang *et al.* confined $Sn_3(PO_4)_2$ nanocrystal in an interconnect carbon framework [$Sn_3(PO_4)_2$@PC] through a controllable particle attachment crystallization growing process of Sn-based phosphate MOFs and high-temperature calcination strategies[47]. As displayed in Figure 7G, the peaks at 986 cm^{-1} shifted to 936 cm^{-1} during potassiation, indicating that $Sn_3(PO_4)_2$ reacted with K to form K_3PO_4. Moreover, the peak of $Sn_3(PO_4)_2$ reappears when recharged to 3.0 V, indicating that the conversion reaction is reversible.

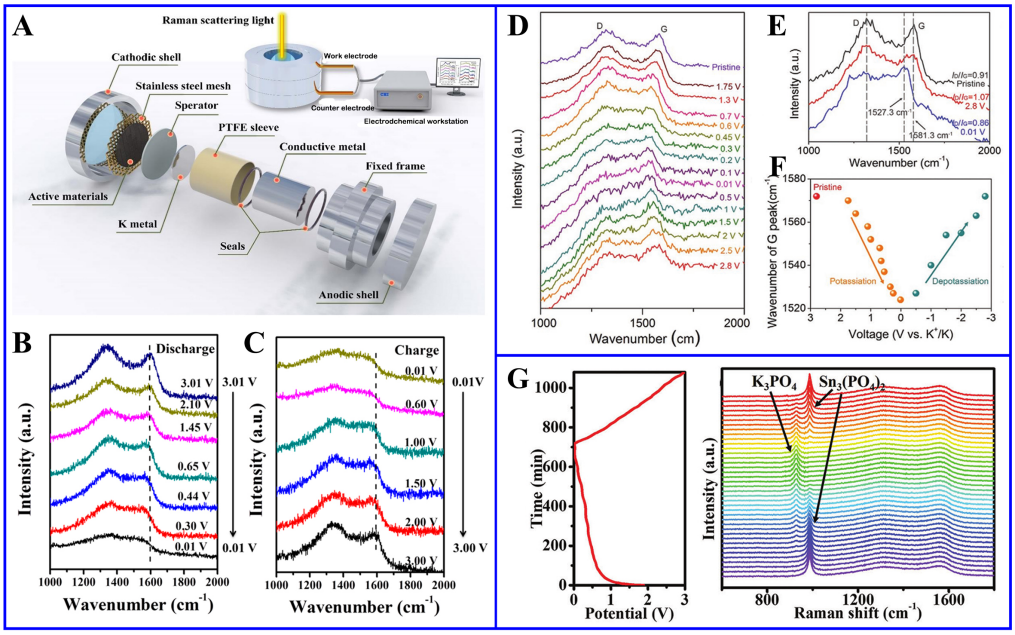

Figure 7. (A) Schematic of *in situ* Raman spectra measurement; (B and C) *In situ* Raman spectra of N-HPC at corresponding voltages. This figure is quoted with permission from Zhou *et al.*[90]. (D) *In situ* Raman spectra of NCS at corresponding voltages; (E) *In situ* Raman spectra and I_D/I_G of NCS at the pristine stage, 2.8 V and 0.01 V; (F) The wavenumber of G peak at corresponding voltages. This figure is quoted with permission from Liang *et al.*[88]. (G) *In situ* Raman spectra of the $Sn_3(PO_4)_2$@PC at different charge/discharge states. This figure is quoted with permission from Jiang *et al.*[47].

In situ XRD

In situ XRD techniques can monitor the structural evolution and phase transition of electrodes in real-time during potassiation/depotassiation, which is conducive to a deeper understanding of the potassium storage mechanism, thus providing clear guidance for the optimization of potassium storage performance. Wu *et al.* used *in situ* XRD techniques to explore the structural evolution of PNCNFs during discharge/charge[100]. Figure 8A exhibited a broad peak (23.27°) at the pristine stage. During discharging, the peak continuously shifted to smaller angles, indicating that K ion intercalation led to the expansion of interlayer spacing. When charged to 2.80 V, the peak recovered to 22.28°, indicating the partially restored interlayer spacing after potassium ion extraction. The incomplete recovery can be attributed to the irreversible capture of K ions. Sun *et al.* also studied the potassium storage mechanism of Bi/carbon composite (Bi@N-CNCs)[139]. Figure 8B exhibited three typical peaks of metal Bi (27.2°, 37.9°, and 39.6°) at the pristine stage. During the first discharging, the peaks of metal Bi gradually decreased. When discharged to 0.40 V, two new peaks appeared at 31.1° and 32.5°, indicating the formation of KBi_2. When the electrode was further discharged to below 0.20 V, two new peaks assigned to K_3Bi appeared at 28.9° and 29.5°, while Bi and KBi_2 diffraction peaks completely disappeared. Therefore, the phase evolution of active Bi in Bi@N-CNCs involved a two-step alloying reaction during the first discharging, which can be described as Bi→KBi_2→K_3Bi [Figure 8C]. During the subsequent charging process, the three recognizable stages indicated a three-step dealloying reaction from K_3Bi to metal Bi. The extraction of K ions in K_3Bi first occurred at 0.55 V with the formation of K_3Bi_2. When charged to about 0.70 V, K_3Bi_2 gradually evolved to KBi_2. Finally, metal Bi was recovered with the disappearance of KBi_2 at about 1.10 V.

In situ TEM

With the development of aberration correction instruments, monochromators, and other instruments, TEM has achieved unprecedented spatial and temporal resolution and multifunctional external field and has

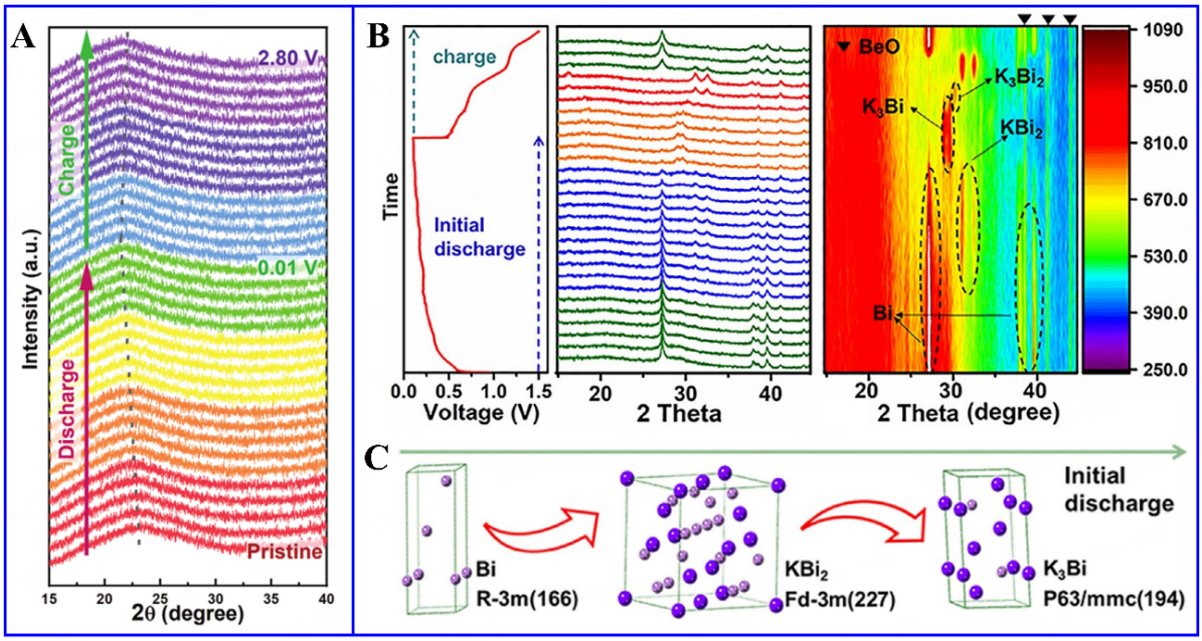

Figure 8. (A) *In situ* XRD patterns of PNCNFs during the discharge/charge process. This figure is quoted with permission from Wang *et al.*[92]. (B) *In situ* XRD patterns of Bi@N-CNCs during the first discharge/charge process; (C) Schematics of the phase change during the first discharge process. This figure is quoted with permission from Hu *et al.*[124].

become one of the most commonly used and powerful tools in the static characterization and dynamic manipulation of materials[152,153]. In order to carry out the charge/discharge reaction and monitor the dynamic morphology and phase evolution in real time to explore the reaction mechanism of electrode materials, the *in situ* TEM technique was developed to supplement the *in situ* Raman and XRD techniques. For example, Sun *et al.* explored the microstructure/morphology changes of Bi/carbon composite (Bi@N-CNCs) during discharging/charging[139]. As shown in Figure 9A, Bi@N-CNCs, metal K, and K_2O grown on the surface of metal potassium were used as the working electrode, counter electrode, and solid electrolyte of *in situ* TEM battery devices. During potassiation [Figure 9B-D], K ions first entered the N-CNC skeleton and then reacted with Bi nanoparticles through alloying reaction, along with increased Bi nanoparticle sizes from about 26 nm to about 39 nm. The expanded Bi nanoparticles filled the internal space of N-CNCs, increasing the length of the carbon skeleton from 195 nm to 201 nm, proving the excellent structural stability of carbon frameworks. During depotassiation [Figure 9E-G], the dealloying reaction occurred with the size of Bi nanoparticles and carbon skeleton returning to 22 nm and 191 nm, respectively. The phase evolution of Bi@N-CNCs during the first potassiation was further studied by *in situ* selected area electron diffraction (SAED). Figure 9H-J exhibited that the phase evolution of active Bi in Bi@N-CNCs involved a two-step alloying reaction, which can be described as $Bi \rightarrow KBi_2 \rightarrow K_3Bi$. Huang *et al.* employed *in situ* TEM to reveal morphological changes of Sb/carbon composite (Sb@CNFs) during potassiation/depotassiation[142]. The internal Sb nanoparticles have significant volume expansion during the alloying reaction. Fortunately, the internal space effectively mitigated the overall volume expansion, while the outer carbon shell avoided the framework collapse, which fully demonstrated the advantages of nanostructure engineering and carbon modification strategies in the alloying-type PIB anodes.

Summary

The working mechanism of MOF-derived carbon is mainly attributed to K ions adsorption on surface-active sites and filling into nanopores due to their high specific surface area and abundant pores, while

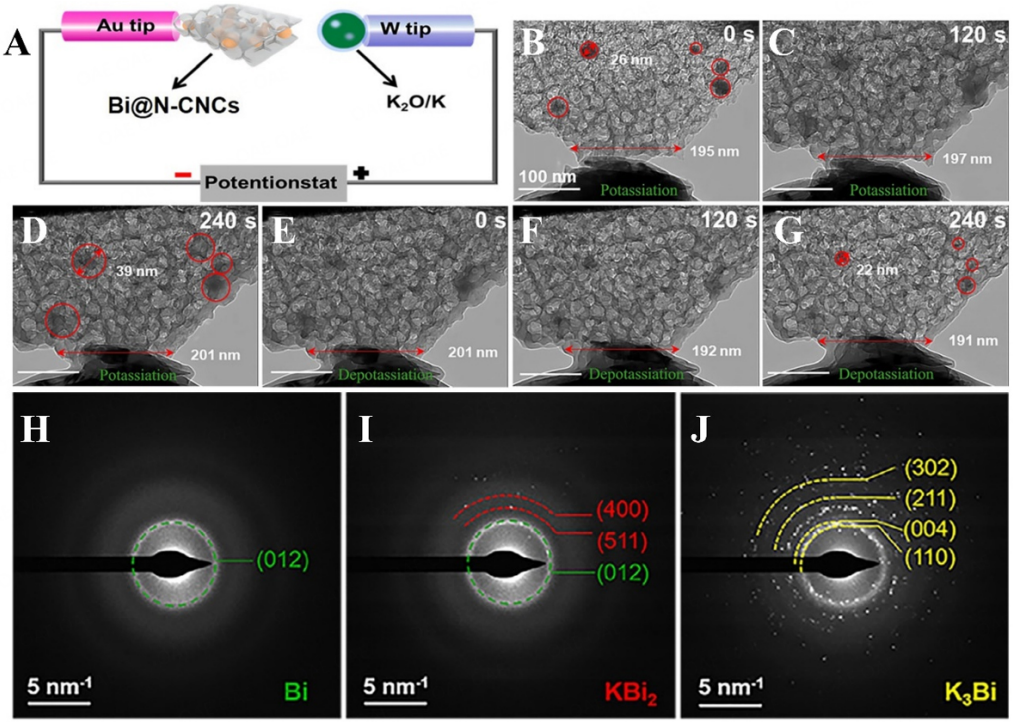

Figure 9. (A) Schematics of *in situ* TEM battery devices; (B-G) *In situ* TEM images of Bi@N-CNCs during potassiation/depotassiation; (H-J) *In situ* SAED images of Bi@N-CNCs during first potassiation. This figure is quoted with permission from Hu *et al.*[124].

MOF-derived carbon composites undergo corresponding chemical reactions. Here, we summarized the reaction mechanisms of common MOF-derived carbon composites in Table 2. Therefore, *in situ* characterization techniques play a crucial role in revealing the potassium storage mechanism of MOF-derived carbon and its composites. *In situ* Raman, *in situ* XRD, and *in situ* TEM have strong tracking capabilities for the evolution of the chemical structure, crystal structure, and morphology in anode materials. Therefore, it is necessary to combine various *in situ* characterization techniques to fully explore the mechanism. Moreover, other *in situ* characterization techniques, such as *in situ* X-ray scattering, *in situ* atomic force microscopy, *in situ* nuclear magnetic resonance, *in situ* SEM, *etc*., can obtain information on ion transportation dynamics, mechanical properties variation, local chemical environment, and heterogeneous charge transfer rate constants, respectively, but are rarely applied to PIBs[151]. These *in situ* characterization techniques still need to be further explored in PIBs, which is conducive to revealing the mechanism of improved electrochemical performance and guiding the fabrication of advanced MOF-based PIB anodes.

CONCLUSION AND OUTLOOK

To promote the substitution of sustainable and renewable energy sources for harmful fossil fuels and achieve carbon neutrality, developing low-cost, safe, and high-performance energy storage and conversion devices is highly urgent. Although LIBs have been mature and successfully commercialized, the shortage of lithium resources and increasing costs make it difficult to maintain their dominance in research and commercialization. The cost advantage of PIBs makes it possible to implement and even replace LIBs for large-scale applications. However, the electrochemical properties of PIBs are still to be further enhanced to satisfy the requirements of commercial applications. As such, it is urgent to prepare high-performance PIB anode materials through novel processes suitable for industrialization and commercialization. Recently, MOFs have been considered as promising self-sacrificial templates and precursors for preparing advanced

Table 2. The reaction mechanisms of common MOF-derived carbon composites

Materials	Reaction mechanisms	Ref.
Conversion reaction		
TiO_2	$11TiO_2 + 2K^+ + 2e^- \rightarrow Ti_7O_{13} + K_2Ti_4O_9$; $K_2Ti_4O_9 + 2K^+ + 2e^- \rightarrow K_4Ti_4O_9$	[104]
CoP	$CoP + 3K^+ + 3e^- \rightarrow Co + K_3P$	[111]
CoS	$CoP + 2K^+ + 2e^- \rightarrow Co + K_2S$	[113]
FeS_2	$FeS_2 + xK^+ + xe^- \rightarrow K_xFeS_2$; $K_xFeS_2 + (4-x)K^+ + (4-x)e^- \rightarrow Fe + 2K_2S$	[114]
CoSe	$CoSe + xK^+ + xe^- \rightarrow K_xCoSe$; $K_xCoSe + (2-x)K^+ + (2-x)e^- \rightarrow Co + K_2Se$	[125]
$MoSe_2$	$MoSe_2 + xK^+ + xe^- \rightarrow K_xMoSe_2$; $3K_xMoSe_2 + (10-3x)K^+ + (10-3x)e^- \rightarrow 3Mo + 2K_5Se_3$	[128]
Alloying reaction		
Bi	$2Bi + K^+ + e^- \rightarrow KBi_2$; $KBi_2 + 5K^+ + 5e^- \rightarrow 2K_3Bi$	[139]
Sb	$Sb + 3K^+ + 3e^- \rightarrow K_3Sb$	[142]
Red P	$15P + K^+ + e^- \rightarrow KP_{15}$; $11KP_{15} + 34K^+ + 34e^- \rightarrow 15K_3P_{11}$; $6K_3P_{11} + 26K^+ + 26e^- \rightarrow 11K_4P_6$; $K_4P_6 + 2K^+ + 2e^- \rightarrow 6KP$; $3KP + K^+ + e^- \rightarrow K_4P_3$	[144]
Conversion-alloying reaction		
Bi/Bi_3Se_4	$Bi_3Se_4 + 8K^+ + 8e^- \rightarrow 3Bi + 4K_2Se$; $2Bi + K^+ + e^- \rightarrow KBi_2$; $KBi_2 + 5K^+ + 5e^- \rightarrow 2K_3Bi$	[147]
Bi_2O_3	$Bi_2O_3 + 6K^+ + 6e^- \rightarrow 2Bi + 3K_2O$; $Bi + 3K^+ + 3e^- \rightarrow K_3Bi$	[148]
$Sn_3(PO_4)_2$	$Sn_3(PO_4)_2 + 6K^+ + 6e^- \rightarrow 3Sn + 2K_3PO_4$; $23Sn + 4K^+ + 4e^- \rightarrow K_4Sn_{23}$; $K_4Sn_{23} + 19K^+ + 19e^- \rightarrow 23KSn$	[47]

anode materials with controllable composition, morphology, performance, *etc*. In this review, we comprehensively summarize the research progress of MOF-derived carbon and its composites, especially the design strategies and composite types. Furthermore, advanced characterization techniques are highlighted for understanding potassium storage mechanisms.

Although significant progress has been made, there are still some challenges in employing MOF-derived carbon and its composites as PIB anodes. Firstly, MOF derivatives are usually synthesized by high-temperature pyrolysis of MOF precursors, which often leads to uncontrollable morphology collapse and pore plugging, resulting in inferior potassium storage performance. Secondly, for MOF-derived carbon, the capacity is usually less than 400 mAh g^{-1} at a low current density; meanwhile, the rate capability is rarely above 200 mAh g^{-1} at a high current density. Besides, the ICE is usually less than 50%. Thirdly, for MOF-derived carbon composites, the cycle stability is usually less than 1,000 cycles because of the huge volume expansion/contraction during conversion and alloying reaction processes. Finally, the working mechanisms of various anode materials are still unclear, and further exploration is needed to better optimize their potassium storage performance. Thus, major breakthroughs can be achieved in the following aspects:

(1) Composition engineering. Although over 20,000 MOFs have been reported, only a few have been used as precursors for PIB anode materials. Moreover, MOF-derived carbon is mostly synthesized by ZIF-8 and ZIF-67, while the active metals of MOF-derived carbon composites are mostly Zn, Co, Fe, Ni, Bi, *etc*., which greatly limits the development of MOF-derived carbon and its composites. Given the tunable composition of MOFs, there are still plenty of possibilities for preparing MOF-derived carbon and its composites as advanced PIB anodes. For MOF-derived carbon, the selection of organic ligands can accurately synthesize carbon materials doped with different heteroatoms. For MOF-derived carbon composites, most of the current research focuses on single metal compound/carbon composites, with little attention paid to two or more metal compounds/carbon composites. The combination of two different metal compounds can form heterostructures and induce a built-in electric field, thereby improving electron transmission at the interface. In addition, there is almost no research on metal compounds/alloy materials/carbon composites. Therefore, the composition engineering of MOF derivatives deserves more exploration.

(2) Controllable synthesis. The green and controllable synthesis of MOF-derived carbon and its composites is a prerequisite for commercial large-scale production. However, the morphology of MOF precursors may be disrupted due to the high-temperature environment during the pyrolysis process, which affects their performance. Slow heating rate and staged pyrolysis are effective strategies to alleviate the morphology damage of MOF derivatives. Moreover, understanding the precise conversion mechanism of MOF derivatives and the key factors affecting their physicochemical properties is still a huge challenge because of the high-temperature environment during the synthesis. Therefore, it is necessary to conduct a detailed and accurate analysis of MOF derivatives obtained at different temperatures through advanced characterization methods. It is worth noting that simple synthesis processes need to be developed to ensure large-scale production from green and affordable raw materials.

(3) Capacity and ICE enhancement. The capacity and ICE of anode materials are important parameters for evaluating their practical applications. However, currently, the capacity and especially ICE of MOF-derived carbon and its composites are still not ideal. Several suggestions for capacity enhancement are put forward: (i) Rational design of structures and pores, such as interconnected 3D frames and hierarchical porous structures, are conducive to electron transport, ion migration and adsorption; (ii) Combined with the properties of metal sites and organic ligands, heteroatoms can be introduced from the initial synthesis process of MOFs, forming abundant and controllable doping and defects in MOF-derived carbon materials after annealing; and (iii) The combination of hard and soft carbon is expected to achieve high capacity and superior rate performance. Although ICE can be significantly improved by reducing specific surface area and surface defects, this goes against capacity enhancement. Therefore, the ICE enhancement can be alternatively attempted by these steps: (i) Appropriate pre-potassiation strategies, such as electrolyte impregnation, can effectively improve ICE; and (ii) Designing appropriate binders and electrolytes is another effective way to improve ICE.

(4) Cycle life elongation. The cycle life of anode materials is another important performance indicator. However, the cycle stability of MOF-derived carbon composites is usually less than 1,000 cycles because of the huge volume expansion/contraction during conversion and alloying reaction processes. Although external carbon materials play a protective role, it is difficult to accurately control the content and thickness of carbon materials due to the uneven distribution of internal metal compounds and alloying materials. Thus, controllable synthesis of these composite materials still needs to be further explored. In addition, the design of MOF-derived carbon composites mainly focuses on structural optimization and composition diversification but ignores the ratio tuning of carbon contents, which also plays an important role in cycle performance and deserves more attention.

(5) Mechanism understanding. The rise of advanced *in situ* characterization techniques has played a crucial role in revealing K ions storage mechanisms. It is extremely necessary and challenging to further develop *in situ* testing techniques. First, *in situ* battery device needs to be further optimized to adapt to different characterization techniques. Second, it is urgent to develop fast detection techniques with high sensitivity and resolution to provide more insights. Third, most of the current *in situ* technologies are applied to the K ion storage process of electrode materials. Consequently, the evolution of electrolytes and the formation of SEI film and potassium dendrite require further attention. Finally, combining *in situ* testing techniques and theoretical calculations is conducive to a deeper understanding of the K ions storage mechanism both experimentally and theoretically.

In summary, MOF-derived carbon and its composites have shown great potential as PIB anodes; with composition engineering, controllable and scalable synthesis, enhanced capacity and ICE, elongated cycling

stability, and well-understood electrochemical mechanism, MOF-derived carbon and its composites will serve as practical and competitive PIB anodes, implementing the commercialization of PIBs in the foreseeable future.

DECLARATIONS

Authors' contributions

Conceived and wrote the manuscript: Yang L
Reviewed the manuscript: Park S
Reviewed the manuscript, funding acquisition: Chen J, Wang H

Availability of data and materials

Not applicable.

Financial support and sponsorship

This work was supported by the National Natural Science Foundation of China (Nos. 52202320, 22179123), the Taishan Scholar Program of Shandong Province, China (No. tsqn202211048), the Shandong Excellent Young Scientists Fund Program (Overseas) (2023HWYQ-060), the Fundamental Research Funds for the Central Universities (Nos. 862201013153, 202262010), and the Shandong Provincial Natural Science Foundation, China (ZR2020ME038).

Conflicts of interest

All authors declared that there are no conflicts of interest.

Ethical approval and consent to participate

Not applicable.

Consent for publication

Not applicable.

REFERENCES

1. Wang W, Xiong F, Zhu S, Chen J, Xie J, An Q. Defect engineering in molybdenum-based electrode materials for energy storage. *eScience* 2022;2:278-94. DOI
2. Zhang J, Chen Z, Xu T, et al. Vanadium nitride nanoparticles embedded in carbon matrix with pseudocapacitive behavior for high performance lithium-ion capacitors. *Rare Met* 2022;41:2460-9. DOI
3. Li G, Guo S, Xiang B, et al. Recent advances and perspectives of microsized alloying-type porous anode materials in high-performance Li- and Na-ion batteries. *Energy Mater* 2022;2:200020. DOI
4. Wang C, Yan B, Zheng J, et al. Recent progress in template-assisted synthesis of porous carbons for supercapacitors. *Adv Powder Mater* 2022;1:100018. DOI
5. Wei X, Liu B, Chen Z, et al. Recent advances in modulation engineering-enabled metal compounds for potassium-ion storage. *Energy Stor Mater* 2022;51:815-39. DOI
6. Chang H, Wu Y, Han X, Yi T. Recent developments in advanced anode materials for lithium-ion batteries. *Energy Mater* 2021;1:100003. DOI
7. Kang J, Zhao Z, Li H, Meng Y, Hu B, Lu H. An overview of aqueous zinc-ion batteries based on conversion-type cathodes. *Energy Mater* 2022;2:200009. DOI
8. Li X, Wang Y, Lv L, Zhu G, Qu Q, Zheng H. Electroactive organics as promising anode materials for rechargeable lithium ion and sodium ion batteries. *Energy Mater* 2022;2:200014. DOI
9. Mu J, Liu Z, Lai Q, et al. An industrial pathway to emerging presodiation strategies for increasing the reversible ions in sodium-ion batteries and capacitors. *Energy Mater* 2022;2:200043. DOI

10. Xiao Z, Wang X, Meng J, Wang H, Zhao Y, Mai L. Advances and perspectives on one-dimensional nanostructure electrode materials for potassium-ion batteries. *Mater Today* 2022;56:114-34. DOI
11. Huang Y, Haider R, Xu S, Liu K, Ma Z, Yuan X. Recent progress of novel non-carbon anode materials for potassium-ion battery. *Energy Stor Mater* 2022;51:327-60. DOI
12. Yan Y, Zeng T, Liu S, Shu C, Zeng Y. Lithium metal stabilization for next-generation lithium-based batteries: from fundamental chemistry to advanced characterization and effective protection. *Energy Mater* 2023;3:300002. DOI
13. Wu X, Chen Y, Xing Z, et al. Advanced carbon-based anodes for potassium-ion batteries. *Adv Energy Mater* 2019;9:1900343. DOI
14. Yuan F, Li Z, Zhang D, et al. Fundamental understanding and research progress on the interfacial behaviors for potassium-ion battery anode. *Adv Sci* 2022;9:e2200683. DOI PubMed PMC
15. Xiao D, Lv X, Fan J, Li Q, Chen Z. Zn-based batteries for energy storage. *Energy Mater* 2023;3:300007. DOI
16. Liu M, Wang Y, Wu F, et al. Advances in carbon materials for sodium and potassium storage. *Adv Funct Mater* 2022;32:2203117. DOI
17. Wang X, Wang H. Designing carbon anodes for advanced potassium-ion batteries: materials, modifications, and mechanisms. *Adv Powder Mater* 2022;1:100057. DOI
18. Zong W, Guo H, Ouyang Y, et al. Topochemistry-driven synthesis of transition-metal selenides with weakened van der waals force to enable 3D-printed Na-ion hybrid capacitors. *Adv Funct Mater* 2022;32:2110016. DOI
19. Shi Y, Zhu B, Guo X, et al. MOF-derived metal sulfides for electrochemical energy applications. *Energy Stor Mater* 2022;51:840-72. DOI
20. Hong Z, Maleki H, Ludwig T, et al. New insights into carbon-based and MXene anodes for Na and K-ion storage: a review. *J Energy Chem* 2021;62:660-91. DOI
21. Zhang Y, Wang Y, Hou L, Yuan C. Recent progress of carbon-based anode materials for potassium ion batteries. *Chem Rec* 2022;22:e202200072. DOI PubMed
22. Lei H, Li J, Zhang X, et al. A review of hard carbon anode: rational design and advanced characterization in potassium ion batteries. *InfoMat* 2022;4:e12272. DOI
23. Wang H, Ye W, Yang Y, Zhong Y, Hu Y. Zn-ion hybrid supercapacitors: achievements, challenges and future perspectives. *Nano Energy* 2021;85:105942. DOI
24. Tian Z, Chui N, Lian R, et al. Dual anionic vacancies on carbon nanofiber threaded MoSSe arrays: a free-standing anode for high-performance potassium-ion storage. *Energy Stor Mater* 2020;27:591-8. DOI
25. Okoshi M, Yamada Y, Komaba S, Yamada A, Nakai H. Theoretical analysis of interactions between potassium ions and organic electrolyte solvents: a comparison with lithium, sodium, and magnesium ions. *J Electrochem Soc* 2017;164:A54. DOI
26. Jian Z, Luo W, Ji X. Carbon electrodes for K-ion batteries. *J Am Chem Soc* 2015;137:11566-9. DOI PubMed
27. Zhu Y, Wang Y, Wang Y, Xu T, Chang P. Research progress on carbon materials as negative electrodes in sodium- and potassium-ion batteries. *Carbon Energy* 2022;4:1182-213. DOI
28. Wang Z, Hong P, Zhao H, Lei Y. Recent developments and future prospects of transition metal compounds as electrode materials for potassium-ion hybrid capacitors. *Adv Mater Technol* 2023;8:2200515. DOI
29. Imtiaz S, Amiinu IS, Xu Y, Kennedy T, Blackman C, Ryan KM. Progress and perspectives on alloying-type anode materials for advanced potassium-ion batteries. *Mater Today* 2021;48:241-69. DOI
30. Tan W, Wang L, Liu K, et al. Bitumen-derived onion-like soft carbon as high-performance potassium-ion battery anode. *Small* 2022;18:e2203494. DOI
31. Geng C, Chen Y, Sun Z, et al. "Pulverization-reaggregation"-induced *in situ* pore expansion in carbon for fast potassium storage. *J Mater Chem A* 2022;10:22399-407. DOI
32. Liu Z, Wu S, Song Y, et al. Non-negligible influence of oxygen in hard carbon as an anode material for potassium-ion batteries. *ACS Appl Mater Interfaces* 2022;14:47674-84. DOI
33. Wang X, Zhao J, Chen Y, et al. Molybdenum sulfide selenide ultrathin nanosheets anchored on carbon tubes for rapid-charging sodium/potassium-ion batteries. *J Colloid Interface Sci* 2022;628:1041-8. DOI
34. Sun X, Zhang B, Chen M, et al. Space-confined growth of Bi_2Se_3 nanosheets encapsulated in N-doped carbon shell lollipop-like composite for full/half potassium-ion and lithium-ion batteries. *Nano Today* 2022;43:101408. DOI
35. Hao Z, Shi X, Zhu W, et al. Bismuth nanoparticles embedded in a carbon skeleton as an anode for high power density potassium-ion batteries. *Chem Sci* 2022;13:11376-81. DOI PubMed PMC
36. Chang H, Shi L, Chen Y, Wang P, Yi T. Advanced MOF-derived carbon-based non-noble metal oxygen electrocatalyst for next-generation rechargeable Zn-air batteries. *Coord Chem Rev* 2022;473:214839. DOI
37. Xie Q, Ou H, Yang Q, et al. A review on metal-organic framework-derived anode materials for potassium-ion batteries. *Dalton Trans* 2021;50:9669-84. DOI
38. Lin J, Chenna Krishna Reddy R, Zeng C, Lin X, Zeb A, Su C. Metal-organic frameworks and their derivatives as electrode materials for potassium ion batteries: a review. *Coord Chem Rev* 2021;446:214118. DOI
39. Fonseca J, Gong T. Fabrication of metal-organic framework architectures with macroscopic size: a review. *Coord Chem Rev* 2022;462:214520. DOI
40. Liu C, Bai Y, Li W, Yang F, Zhang G, Pang H. In situ growth of three-dimensional MXene/metal-organic framework composites for high-performance supercapacitors. *Angew Chem Int Ed* 2022;61:e202116282. DOI

41. Zhao X, Zheng Y, Dai H, et al. Wet-chemistry: a useful tool for deriving metal-organic frameworks toward supercapacitors and secondary batteries. *Adv Mater Interfaces* 2022;9:2102595. DOI
42. Ren Y, Wang X, Ma J, Zheng Q, Wang L, Jiang W. Metal-organic framework-derived carbon-based composites for electromagnetic wave absorption: dimension design and morphology regulation. *J Mater Sci Technol* 2023;132:223-51. DOI
43. Cao S, Li Y, Tang Y, et al. Space-confined metal ion strategy for carbon materials derived from cobalt benzimidazole frameworks with high desalination performance in simulated seawater. *Adv Mater* 2023;35:e2301011. DOI
44. Shen M, Ma H. Metal-organic frameworks (MOFs) and their derivative as electrode materials for lithium-ion batteries. *Coord Chem Rev* 2022;470:214715. DOI
45. Ye Z, Jiang Y, Li L, Wu F, Chen R. Rational design of MOF-based materials for next-generation rechargeable batteries. *Nanomicro Lett* 2021;13:203. DOI PubMed PMC
46. Zhang Y, Sha M, Fu Q, Zhao H, Lei Y. An overview of metal-organic frameworks-derived carbon as anode materials for sodium- and potassium-ion batteries. *Mater Today Sustain* 2022;18:100156. DOI
47. Jiang H, Zhang S, Yan L, et al. Stress-dispersed superstructure of $Sn_3(PO_4)_2$@PC derived from programmable assembly of metal-organic framework as long-life potassium/sodium-ion batteries anodes. *Adv Sci* 2023;10:e2206587. DOI PubMed PMC
48. Qiu D, Hou Y. Carbon materials toward efficient potassium storage: rational design, performance evaluation and potassium storage mechanism. *Green Energy Environ* 2023;8:115-40. DOI
49. Li Y, Zhang J, Chen M. MOF-derived carbon and composites as advanced anode materials for potassium ion batteries: a review. *Sustain Mater Technol* 2020;26:e00217. DOI
50. Rajagopalan R, Tang Y, Ji X, Jia C, Wang H. Advancements and challenges in potassium ion batteries: a comprehensive review. *Adv Funct Mater* 2020;30:1909486. DOI
51. Li W, Bi Z, Zhang W, et al. Advanced cathodes for potassium-ion batteries with layered transition metal oxides: a review. *J Mater Chem A* 2021;9:8221-47. DOI
52. Hwang J, Myung S, Sun Y. Recent progress in rechargeable potassium batteries. *Adv Funct Mater* 2018;28:1802938. DOI
53. Zhang W, Yin J, Wang W, Bayhan Z, Alshareef HN. Status of rechargeable potassium batteries. *Nano Energy* 2021;83:105792. DOI
54. Jin S, Liang P, Jiang Y, et al. Preferentially engineering edge-nitrogen sites in porous hollow spheres for ultra-fast and reversible potassium storage. *Chem Eng J* 2022;435:134821. DOI
55. Xu C, Mu J, Zhou T, et al. Surface redox pseudocapacitance boosting vanadium nitride for high-power and ultra-stable potassium-ion capacitors. *Adv Funct Mater* 2022;32:2206501. DOI
56. Gao J, Wang G, Wang W, et al. Engineering electronic transfer dynamics and ion adsorption capability in dual-doped carbon for high-energy potassium ion hybrid capacitors. *ACS Nano* 2022;16:6255-65. DOI
57. Chen Y, Shi X, Lu B, Zhou J. Concave engineering of hollow carbon spheres toward advanced anode material for sodium/potassium-ion batteries. *Adv Energy Mater* 2022;12:2202851. DOI
58. Dou S, Tian Q, Liu T, et al. Stress-regulation design of mesoporous carbon spheres anodes with radial pore channels toward ultrastable potassium-ion batteries. *Small Sci* 2022;2:2200045. DOI
59. Cheng G, Zhang W, Wang W, et al. Sulfur and nitrogen codoped cyanoethyl cellulose-derived carbon with superior gravimetric and volumetric capacity for potassium ion storage. *Carbon Energy* 2022;4:986-1001. DOI
60. Cheng N, Zhou W, Liu J, Liu Z, Lu B. Reversible oxygen-rich functional groups grafted 3D honeycomb-like carbon anode for super-long potassium ion batteries. *Nanomicro Lett* 2022;14:146. DOI PubMed PMC
61. Zhang X, Han R, Liu Y, et al. Porous and graphitic structure optimization of biomass-based carbon materials from 0D to 3D for supercapacitors: a review. *Chem Eng J* 2023;460:141607. DOI
62. Chen D, Zhang W, Luo K, et al. Hard carbon for sodium storage: mechanism and optimization strategies toward commercialization. *Energy Environ Sci* 2021;14:2244-62. DOI
63. Zhang M, Li Y, Wu F, Bai Y, Wu C. Boost sodium-ion batteries to commercialization: strategies to enhance initial coulombic efficiency of hard carbon anode. *Nano Energy* 2021;82:105738. DOI
64. Zhang Z, Duan L, Li A, Xu J, Shen J, Zhou X. Layered oxide cathodes promoted by crystal regulation strategies for potassium-ion batteries. *Chemistry* 2022;28:e202201562. DOI PubMed
65. Nathan MGT, Yu H, Kim GT, et al. Recent advances in layered metal-oxide cathodes for application in potassium-ion batteries. *Adv Sci* 2022;9:e2105882. DOI PubMed PMC
66. Cao B, Zhang Q, Liu H, et al. Graphitic carbon nanocage as a stable and high power anode for potassium-ion batteries. *Adv Energy Mater* 2018;8:1801149. DOI
67. Bi H, He X, Yang L, Li H, Jin B, Qiu J. Interconnected carbon nanocapsules with high N/S co-doping as stable and high-capacity potassium-ion battery anode. *J Energy Chem* 2022;66:195-204. DOI
68. Zhang X, Chen D, Zhou Y, et al. Mesoporous carbon nanosheet-assembled flowers towards superior potassium storage. *Chinese Chem Lett* 2021;32:1161-4. DOI
69. Liu H, Du H, Zhao W, et al. Fast potassium migration in mesoporous carbon with ultrathin framework boosting superior rate performance for high-power potassium storage. *Energy Stor Mater* 2021;40:490-8. DOI
70. Suo G, Li D, Feng L, Hou X, Yang Y, Wang W. SnO_2 nanosheets grown on stainless steel mesh as a binder free anode for potassium ion batteries. *J Electroanal Chem* 2019;833:113-8. DOI
71. Liu T, Zhang X, Xia M, et al. Functional cation defects engineering in TiS_2 for high-stability anode. *Nano Energy* 2020;67:104295.

DOI

72. Huang J, Lin X, Tan H, Zhang B. Bismuth microparticles as advanced anodes for potassium-ion battery. *Adv Energy Mater* 2018;8:1703496. DOI
73. Yang Y, Li D, Zhang J, et al. Sn nanoparticles anchored on N doped porous carbon as an anode for potassium ion batteries. *Mater Lett* 2019;256:126613. DOI
74. Huang X, Liu D, Guo X, Sui X, Qu D, Chen J. Phosphorus/carbon composite anode for potassium-ion batteries: insights into high initial coulombic efficiency and superior cyclic performance. *ACS Sustain Chem Eng* 2018;6:16308-14. DOI
75. Yuan F, Shi C, Li Q, et al. Unraveling the effect of intrinsic carbon defects on potassium storage performance. *Adv Funct Mater* 2022;32:2208966. DOI
76. Wang H, Du H, Zhang H, et al. Regulated adsorption-diffusion and enhanced charge transfer in expanded graphite cohered with N, B bridge-doping carbon patches to boost K-ion storage. *J Energy Chem* 2023;76:67-74. DOI
77. Yang B, Li B, Xiang Z. Advanced MOF-based electrode materials for supercapacitors and electrocatalytic oxygen reduction. *Nano Res* 2023;16:1338-61. DOI
78. Lu XF, Xia BY, Zang SQ, Lou XWD. Metal-organic frameworks based electrocatalysts for the oxygen reduction reaction. *Angew Chem Int Ed* 2020;59:4634-50. DOI PubMed
79. Xiong P, Zhao X, Xu Y. Nitrogen-doped carbon nanotubes derived from metal-organic frameworks for potassium-ion battery anodes. *ChemSusChem* 2018;11:202-8. DOI
80. Li D, Cheng X, Xu R, et al. Manipulation of 2D carbon nanoplates with a core-shell structure for high-performance potassium-ion batteries. *J Mater Chem A* 2019;7:19929-38. DOI
81. Liu S, Yang B, Zhou J, Song H. Nitrogen-rich carbon-onion-constructed nanosheets: an ultrafast and ultrastable dual anode material for sodium and potassium storage. *J Mater Chem A* 2019;7:18499-509. DOI
82. Shao M, Li C, Li T, et al. Pushing the energy output and cycling lifespan of potassium-ion capacitor to high level through metal-organic framework derived porous carbon microsheets anode. *Adv Funct Mater* 2020;30:2006561. DOI
83. Zheng G, Xing Z, Gao X, Nie C, Xu Z, Ju Z. Fabrication of 2D Cu-BDC MOF and its derived porous carbon as anode material for high-performance Li/K-ion batteries. *Appl Surf Sci* 2021;559:149701. DOI
84. Zhang W, Jiang X, Wang X, et al. Spontaneous weaving of graphitic carbon networks synthesized by pyrolysis of ZIF-67 crystals. *Angew Chem Int Ed* 2017;56:8435-40. DOI
85. Li Y, Zhong W, Yang C, et al. N/S codoped carbon microboxes with expanded interlayer distance toward excellent potassium storage. *Chem Eng J* 2019;358:1147-54. DOI
86. Liu C, Wang J, Wan J, Yu C. MOF-on-MOF hybrids: synthesis and applications. *Coord Chem Rev* 2021;432:213743. DOI
87. Yu D, Song Q, Cui J, et al. Designing core-shell metal-organic framework hybrids: toward high-efficiency electrochemical potassium storage. *J Mater Chem A* 2021;9:26181-8. DOI
88. Liang Z, Wu Y, Cheng J, et al. A metal-organic framework nanorod-assembled superstructure and its derivative: unraveling the fast potassium storage mechanism in nitrogen-modified micropores. *Small* 2021;17:e2100135. DOI
89. Yuan F, Wang J, Wang H, et al. Dual-carbon coupled three-dimensional superstructures with dominant mesopores targeting fast potassium-ion storage. *Compos Part B Eng* 2023;248:110379. DOI
90. Zhou X, Chen L, Zhang W, et al. Three-dimensional ordered macroporous metal-organic framework single crystal-derived nitrogen-doped hierarchical porous carbon for high-performance potassium-ion batteries. *Nano Lett* 2019;19:4965-73. DOI
91. Ruan J, Mo F, Chen Z, et al. Rational construction of nitrogen-doped hierarchical dual-carbon for advanced potassium-ion hybrid capacitors. *Adv Energy Mater* 2020;10:1904045. DOI
92. Wang B, Gu L, Yuan F, et al. Edge-enrich N-doped graphitic carbon: boosting rate capability and cyclability for potassium ion battery. *Chem Eng J* 2022;432:134321. DOI
93. Yang J, Ju Z, Jiang Y, et al. Enhanced capacity and rate capability of nitrogen/oxygen dual-doped hard carbon in capacitive potassium-ion storage. *Adv Mater* 2018;30:1700104. DOI
94. Li Y, Yang C, Zheng F, et al. High pyridine N-doped porous carbon derived from metal-organic frameworks for boosting potassium-ion storage. *J Mater Chem A* 2018;6:17959-66. DOI
95. Tong H, Wang C, Lu J, et al. Energetic metal-organic frameworks derived highly nitrogen-doped porous carbon for superior potassium storage. *Small* 2020;16:e2002771. DOI
96. Chen M, Wang W, Liang X, et al. Sulfur/oxygen codoped porous hard carbon microspheres for high-performance potassium-ion batteries. *Adv Energy Mater* 2018;8:1800171. DOI
97. Li J, Qin W, Xie J, et al. Sulphur-doped reduced graphene oxide sponges as high-performance free-standing anodes for K-ion storage. *Nano Energy* 2018;53:415-24. DOI
98. Zuo Y, Li P, Zang R, et al. Sulfur-doped flowerlike porous carbon derived from metal-organic frameworks as a high-performance potassium-ion battery anode. *ACS Appl Energy Mater* 2021;4:2282-91. DOI
99. Hu X, Zhong G, Li J, et al. Hierarchical porous carbon nanofibers for compatible anode and cathode of potassium-ion hybrid capacitor. *Energy Environ Sci* 2020;13:2431-40. DOI
100. Wu Y, Cheng J, Liang Z, et al. Puffing up hollow carbon nanofibers with high-energy metal-organic frameworks for capacitive-dominated potassium-ion storage. *Small* 2022;18:e2105767. DOI
101. Zhu Z, Li X, Zhang Z, et al. N/S codoping modification based on the metal organic framework-derived carbon to improve the

electrochemical performance of different energy storage devices. *J Energy Chem* 2022;74:394-403. DOI

102. Lu J, Wang C, Yu H, et al. Oxygen/fluorine dual-doped porous carbon nanopolyhedra enabled ultrafast and highly stable potassium storage. *Adv Funct Mater* 2019;29:1906126. DOI
103. Hu J, Guan C, Li H, et al. Boosting potassium-storage performance via confining highly dispersed molybdenum dioxide nanoparticles within N-doped porous carbon nano-octahedrons. *J Colloid Interface Sci* 2022;607:1109-19. DOI
104. Dubal DP, Schneemann A, Ranc V, et al. Ultrafine TiO_2 nanoparticle supported nitrogen-rich graphitic porous carbon as an efficient anode material for potassium-ion batteries. *Adv Energy Sustain Res* 2021;2:2100042. DOI
105. Wang Q, Kang L, Xing Z, et al. Prussian blue analogue-derived ZnO/$ZnFe_2O_4$ core-shell nanospheres as high-performance anodes for lithium-ion and potassium-ion batteries. *Batteries Supercaps* 2023;6:e202200411. DOI
106. Li H, Chen J, Zhang L, et al. A metal-organic framework-derived pseudocapacitive titanium oxide/carbon core/shell heterostructure for high performance potassium ion hybrid capacitors. *J Mater Chem A* 2020;8:16302-11. DOI
107. Zhang Z, Wu C, Chen Z, et al. Spatially confined synthesis of a flexible and hierarchically porous three-dimensional graphene/FeP hollow nanosphere composite anode for highly efficient and ultrastable potassium ion storage. *J Mater Chem A* 2020;8:3369-78. DOI
108. Das D, Sarkar D, Nagarajan S, Mitlin D. Cobalt phosphide (Co_2P) encapsulated in nitrogen-rich hollow carbon nanocages with fast rate potassium ion storage. *Chem Commun* 2020;56:14889-92. DOI PubMed
109. Jiang Y, Liang J, Yue L, et al. Reduced graphene oxide supported ZIF-67 derived CoP enables high-performance potassium ion storage. *J Colloid Interface Sci* 2021;604:319-26. DOI
110. Miao W, Zhao X, Wang R, et al. Carbon shell encapsulated cobalt phosphide nanoparticles embedded in carbon nanotubes supported on carbon nanofibers: A promising anode for potassium ion battery. *J Colloid Interface Sci* 2019;556:432-40. DOI
111. Yi Y, Zhao W, Zeng Z, et al. ZIF-8@ZIF-67-derived nitrogen-doped porous carbon confined CoP polyhedron targeting superior potassium-ion storage. *Small* 2020;16:e1906566. DOI
112. Chen J, Chua DHC, Lee PS. The advances of metal sulfides and in situ characterization methods beyond li ion batteries: sodium, potassium, and aluminum ion batteries. *Small Methods* 2020;4:1900648. DOI
113. Miao W, Zhang Y, Li H, et al. ZIF-8/ZIF-67-derived 3D amorphous carbon-encapsulated CoS/NCNTs supported on CoS-coated carbon nanofibers as an advanced potassium-ion battery anode. *J Mater Chem A* 2019;7:5504-12. DOI
114. Zhou X, Wang Z, Wang Y, et al. Graphene supported FeS_2 nanoparticles with sandwich structure as a promising anode for high-rate potassium-ion batteries. *J Colloid Interface Sci* 2023;636:73-82. DOI
115. Choi S, Hwan Kim Y, Lee G, Seok Choi H, Kim K. MOF-derived carbon/ZnS nanoparticle composite interwoven with structural and conductive CNT scaffolds for ultradurable K-ion storage. *Chem Eng J* 2023;459:141663. DOI
116. Rui B, Li J, Chang L, et al. Engineering MoS_2 nanosheets anchored on metal organic frameworks derived carbon polyhedra for superior lithium and potassium storage. *Front Energy Res* 2019;7:142. DOI
117. Jiang Q, Wang L, Chen J, et al. Enhancing potassium-ion battery performance by MoS_2 coated nitrogen-doped hollow carbon matrix. *J Alloy Compd* 2021;855:157505. DOI
118. Hu C, Ma K, Hu Y, et al. Confining MoS_2 nanocrystals in MOF-derived carbon for high performance lithium and potassium storage. *Green Energy Environ* 2021;6:75-82. DOI
119. Cai J, Liu C, Tao S, et al. MOFs-derived advanced heterostructure electrodes for energy storage. *Coord Chem Rev* 2023;479:214985. DOI
120. Li X, Liang H, Qin B, Wang M, Zhang Y, Fan H. Rational design of heterostructured bimetallic sulfides (CoS_2/NC@VS_4) with VS_4 nanodots decorated on CoS_2 dodecahedron for high-performance sodium and potassium ion batteries. *J Colloid Interface Sci* 2022;625:41-9. DOI
121. Zhang B, Xu B, Qin H, Cao L, Ou X. Highly active and stable Cu_9S_5-MoS_2 heterostructures nanocages enabled by dual-functional Cu electrocatalyst with enhanced potassium storage. *J Mater Sci Technol* 2023;143:107-16. DOI
122. Ma G, Li C, Liu F, et al. Metal-organic framework-derived $Co_{0.85}Se$ nanoparticles in N-doped carbon as a high-rate and long-lifespan anode material for potassium ion batteries. *Mater Today Energy* 2018;10:241-8. DOI
123. He Y, Wang L, Dong C, et al. In-situ rooting ZnSe/N-doped hollow carbon architectures as high-rate and long-life anode materials for half/full sodium-ion and potassium-ion batteries. *Energy Stor Mater* 2019;23:35-45. DOI
124. Hu Y, Lu T, Zhang Y, et al. Highly dispersed ZnSe nanoparticles embedded in N-doped porous carbon matrix as an anode for potassium ion batteries. *Part Part Syst Charact* 2019;36:1900199. DOI
125. Huang Q, Fan X, Ou X, Wang H, Wu L, Yang C. Fabrication of CoSe@NC nanocubes for high performance potassium ion batteries. *J Colloid Interface Sci* 2021;604:157-67. DOI
126. Kim M, Kim JH, Kang YC. Solution-phase selenization engineering of zeolitic imidazolate framework (ZIF)-67-derived $Co_{0.85}Se$@nitrogen-doped carbon for potassium-ion storage. *Appl Surf Sci* 2023;614:156218. DOI
127. Wang H, Yu K, Wang P, Jia P, Yuan Y, Liang C. ZIF-67-derived Co/CoSe ultrafine nanocrystal Schottky heterojunction decorated hollow carbon nanospheres as new-type anodes for potassium-ion batteries. *J Colloid Interface Sci* 2023;645:55-65. DOI
128. Jiang Q, Wang L, Wang Y, et al. Rational design of $MoSe_2$ nanosheet-coated MOF-derived N-doped porous carbon polyhedron for potassium storage. *J Colloid Interface Sci* 2021;600:430-9. DOI
129. Na J, Chan Kang Y, Park S. Electrospun MOF-based ZnSe nanocrystals confined in N-doped mesoporous carbon fibers as anode materials for potassium ion batteries with long-term cycling stability. *Chem Eng J* 2021;425:131651. DOI
130. Wang L, Jiang Q, Yang K, et al. Self-assembly of carbon nanotubes on a hollow carbon polyhedron to enhance the potassium storage

cycling stability of metal organic framework-derived metallic selenide anodes. *J Colloid Interface Sci* 2021;601:60-9. DOI

131. Liu L, Meng X, Hu L, et al. Regular mesoporous structural FeSe@C composite with enhanced reversibility for fast and stable potassium storage. *J Phys Chem C* 2021;125:15812-20. DOI
132. Yang SH, Park SK, Kang YC. MOF-derived $CoSe_2$@N-doped carbon matrix confined in hollow mesoporous carbon nanospheres as high-performance anodes for potassium-ion batteries. *Nanomicro Lett* 2020;13:9. DOI PubMed PMC
133. Ruan J, Zang J, Hu J, et al. Respective roles of inner and outer carbon in boosting the K^+ storage performance of dual-carbon-confined ZnSe. *Adv Sci* 2022;9:e2104822. DOI PubMed PMC
134. Oh HG, Park S. Co-MOF derived $MoSe_2$@$CoSe_2$/N-doped carbon nanorods as high-performance anode materials for potassium ion batteries. *Int J Energy Res* 2022;46:10677-88. DOI
135. Zhou P, Zhang M, Wang L, et al. MOFs-derived flower-like hierarchically porous Zn-Mn-Se/C composite for extraordinary rate performance and durable anode of sodium-ion and potassium-ion batteries. *Small* 2022;18:e2203964. DOI
136. Yan C, Gu X, Zhang L, et al. Highly dispersed Zn nanoparticles confined in a nanoporous carbon network: promising anode materials for sodium and potassium ion batteries. *J Mater Chem A* 2018;6:17371-7. DOI
137. Gu Y, Ru Pei Y, Zhao M, Cheng Yang C, Jiang Q. Sn-, Sb- and Bi-based anodes for potassium ion battery. *Chem Rec* 2022;22:e202200098. DOI PubMed
138. Su S, Liu Q, Wang J, et al. Control of SEI formation for stable potassium-ion battery anodes by Bi-MOF-derived nanocomposites. *ACS Appl Mater Interfaces* 2019;11:22474-80. DOI
139. Sun Z, Liu Y, Ye W, et al. Unveiling intrinsic potassium storage behaviors of hierarchical nano Bi@N-doped carbon nanocages framework via in situ characterizations. *Angew Chem Int Ed* 2021;60:7180-7. DOI
140. Tong H, Chen S, Tu J, et al. Bi_2O_3 particles embedded in carbon matrix as high-performance anode materials for potassium ion batteries. *J Power Sources* 2022;549:232140. DOI
141. Cheng N, Zhao J, Fan L, et al. Sb-MOFs derived Sb nanoparticles@porous carbon for high performance potassium-ion batteries anode. *Chem Commun* 2019;55:12511-4. DOI
142. Huang H, Wang J, Yang X, et al. Unveiling the advances of nanostructure design for alloy-type potassium-ion battery anodes via in situ TEM. *Angew Chem Int Ed* 2020;132:14612-8. DOI
143. Zeng L, Huang L, Zhu J, et al. Phosphorus-based materials for high-performance alkaline metal ion batteries: progress and prospect. *Small* 2022;18:e2201808. DOI
144. Sui X, Huang X, Pu H, Wang Y, Chen J. Tailoring MOF-derived porous carbon nanorods confined red phosphorous for superior potassium-ion storage. *Nano Energy* 2021;83:105797. DOI
145. Liang Z, Qiu T, Cheng J, et al. Nano-confining red phosphorus in a carbon hierarchical superstructure for superior potassium storage. *Batteries Supercaps* 2021;5:e202100264. DOI
146. Chen K, Chong S, Yuan L, Yang Y, Tuan H. Conversion-alloying dual mechanism anode: nitrogen-doped carbon-coated Bi_2Se_3 wrapped with graphene for superior potassium-ion storage. *Energy Stor Mater* 2021;39:239-49. DOI
147. Chen Z, Wu Y, Liu X, Zhang Y, Yang L, Li H. Bi/Bi_3Se_4 nanoparticles embedded in hollow porous carbon nanorod: high rate capability material for potassium-ion batteries. *J Energy Chem* 2023;81:462-71. DOI
148. Zhang P, Wei Y, Zhou S, Soomro RA, Jiang M, Xu B. A metal-organic framework derived approach to fabricate *in-situ* carbon encapsulated Bi/Bi_2O_3 heterostructures as high-performance anodes for potassium ion batteries. *J Colloid Interface Sci* 2023;630:365-74. DOI
149. Tong Z, Kang T, Wu Y, Zhang F, Tang Y, Lee C. Novel metastable Bi:Co and Bi:Fe alloys nanodots@carbon as anodes for high rate K-ion batteries. *Nano Res* 2022;15:7220-6. DOI
150. Xu Y, Titirici M, Chen J, et al. 2023 roadmap for potassium-ion batteries. *J Phys Energy* 2023;5:021502. DOI
151. Chen J, Lee PS. Electrochemical supercapacitors: from mechanism understanding to multifunctional applications. *Adv Energy Mater* 2021;11:2003311. DOI
152. Luo C, Wang C, Wu X, Zhang J, Chu J. In situ transmission electron microscopy characterization and manipulation of two-dimensional layered materials beyond graphene. *Small* 2017;13:1604259. DOI
153. Cui J, Zheng H, He K. In situ TEM study on conversion-type electrodes for rechargeable ion batteries. *Adv Mater* 2021;33:e2000699. DOI